Adaptive and Fast Combined Waveform-Beamforming Design for MMWave Automotive Joint Communication-Radar

Kumari, Preeti; Myers, Nitin Jonathan; Heath, Robert W.

DOI
10.1109/JSTSP.2021.3071592

Publication date
2021

Document Version
Final published version

Published in
IEEE Journal on Selected Topics in Signal Processing

Citation (APA)
Kumari, P., Myers, N. J., & Heath, R. W. (2021). Adaptive and Fast Combined Waveform-Beamforming Design for MMWave Automotive Joint Communication-Radar. *IEEE Journal on Selected Topics in Signal Processing*, *15*(4), 996-1012. https://doi.org/10.1109/JSTSP.2021.3071592

Adaptive and Fast Combined Waveform-Beamforming Design for MMWave Automotive Joint Communication-Radar

Preeti Kumari, *Member, IEEE*, Nitin Jonathan Myers, *Member, IEEE*, and Robert W. Heath, *Fellow, IEEE*

***Abstract*—Millimeter-wave (mmWave) joint communication-radar (JCR) will enable high data rate communication and high-resolution radar sensing for applications such as autonomous driving. Prior JCR systems that are based on the mmWave communications hardware, however, suffer from a limited angular field-of-view and low estimation accuracy for radars due to the employed directional communication beam. In this paper, we propose an adaptive and fast combined waveform-beamforming design for the mmWave automotive JCR with a phased-array architecture that permits a trade-off between communication and radar performances. To rapidly estimate the mmWave automotive radar channel in the Doppler-angle domain with a wide field-of-view, our JCR design employs circulant shifts of the transmit beamformer to acquire radar channel measurements and uses two-dimensional compressed sensing (CS) in the space-time dimension. We optimize these circulant shifts to minimize the coherence of the CS matrix, under the space-time sampling constraints in our problem. We evaluate the JCR performance trade-offs using a normalized mean square error (MSE) metric for radar estimation and a distortion MSE metric for data communication, which is analogous to the distortion metric in the rate-distortion theory. Additionally, we develop a MSE-based weighted average optimization problem for the adaptive JCR combined waveform-beamforming design. Numerical results demonstrate that our proposed JCR design enables the estimation of short- and medium-range radar channels in the Doppler-angle domain with a low normalized MSE, at the expense of a small degradation in the communication distortion MSE.**

***Index Terms*—Automotive radar, millimeter-wave vehicular communication, joint communication-radar, partial Fourier compressed sensing, adaptive waveform and beamforming design.**

I. INTRODUCTION

MILLIMETER-WAVE (mmWave) communication and radar are key technologies for many next-generation applications, such as autonomous driving. MmWave automotive radars provide high-resolution sensing with a wide field of view (FoV) [1], while mmWave communications will enable a high data rate solution for the next-generation connected vehicles [2]. The combination of these two technologies into a single joint communication-radar (JCR) enables hardware reuse and a common signaling waveform. This leads to benefits in power consumption, spectrum efficiency, and market penetrability. Unfortunately, a fully-digital multiple-input-multiple-output mmWave JCR with high-speed, high-resolution analog-to-digital converters will result in huge power consumption and high hardware complexity due to the wide available bandwidth and large antenna array.

To mitigate these issues, we propose an adaptive and fast combined waveform-beamforming design for the mmWave automotive JCR that uses a phased-array architecture with phase only control. Such an architecture is used in the mmWave WLAN IEEE 802.11ad standard [3]. In this design, we exploit all the transmit (TX) antennas during the data transmission mode to construct a narrow coherent beam for communication and constant gain sidelobes in other directions for radar sensing. Then, the transmitter applies circulant shifts of the designed TX beamformer, and employs two-dimensional (2D) partial Fourier compressed sensing (CS) technique to rapidly estimate the Doppler-angle domain radar channel. To achieve better radar channel reconstruction with CS, we optimize the sequence of circulant shifts used at the TX. Additionally, we use a generic JCR TX waveform structure with tunable preamble length to increase the range for automotive radar sensing. Then, we develop a mean square error (MSE)-based adaptive combined waveform-beamforming design for the mmWave automotive JCR to find the optimal mainlobe gain for communication and the optimal preamble length to achieve high channel estimation accuracy for medium-range radar (MRR) and short-range radar (SRR), at the cost of a small reduction in the vehicle-to-vehicle (V2V) communication rate.

Most prior work on mmWave automotive JCR systems are either radar-centric or communication-centric [4], [5]. In the radar-centric JCR, the communication messages are modulated on top of the radar waveforms [6], or the communication information

---

Manuscript received September 5, 2020; revised January 31, 2021 and March 21, 2021; accepted March 28, 2021. Date of publication April 7, 2021; date of current version June 3, 2021. This work was supported in part by National Science Foundation under Grant ECCS-1711702 and in part by Army Research Office under Grant W911NF1910221. The guest editor coordinating the review of this manuscript and approving it for publication was M. Torlak *(Corresponding author: Preeti Kumari.)*

Preeti Kumari was with Wireless Networking and Communications Group, The University of Texas at Austin, Austin, TX 78712 USA and is now with Qualcomm Technologies Inc., San Diego, CA 92121 USA (e-mail: preeti_kumari@utexas.edu).

Nitin Jonathan Myers was with Wireless Networking and Communications Group, The University of Texas at Austin, Austin, TX 78712 USA and is now with the Delft Center for Systems and Control, Delft University of Technology, 2628 CD Delft, The Netherlands (e-mail: N.J.Myers@tudelft.nl).

Robert W. Heath was with Wireless Networking and Communications Group, The University of Texas at Austin, Austin, TX 78712 USA and is now with the Department of Electrical and Computer Engineering, North Carolina State University, Raleigh, NC 27606 USA (e-mail: rwheathjr@ncsu.edu).

Digital Object Identifier 10.1109/JSTSP.2021.3071592

is embedded in the TX beamforming vectors [7]. These systems, however, do not support high data rates as the communication signal must be spread to avoid disturbing the radar required properties and they employ analog pre-processing in the time-domain. In [8], a communication-centric mmWave automotive JCR with fully-digital time-domain processing was developed by exploiting the preamble of the IEEE 802.11ad standard [3]. Using simulations, it was shown that IEEE 802.11ad-based JCR can simultaneously achieve high range/velocity resolution for automotive long-range radar (LRR) sensing and gigabits-per-second data rates for V2V communications. The IEEE 802.11ad standard, however, supports single-stream analog beamforming that leads to a large trade-off between communication and radar performances.

Prior approaches to increase the radar FoV for mmWave automotive JCR using phased array architecture with phase only control can be categorized into two types: (a) JCR during the communication beam training mode and (b) JCR with an adaptive beamforming design during the data transmission mode. In the first approach [9], [10], the communication beam training mode was proposed for radar sensing. In [9], the IEEE 802.11ad beam scanning algorithm was exploited for radar detection/estimation with a wide FoV. In [10], a new MAC configuration for vehicle-to-infrastructure JCR application was proposed that employed beam switching pattern with dedicated sectors for radar and communication. In the second approach [11], the IEEE 802.11ad SC PHY frames along with the adaptive random switching (RS) of TX antennas during the data transmission mode was proposed. In the RS-JCR, a coherent beam is formed towards the communication receiver, while simultaneously perturbing the grating lobes of the resulting beam pattern for angle-of-arrival (AoA) estimation in SRR applications. The RS-JCR has a higher radar update rate than the first approach, and is based on a commercially available mmWave hardware. The RS-JCR, however, employs TX antenna subsets instead of using all antennas, which decreases the net TX power for JCR operation under a per-antenna power constraint. Additionally, the RS-JCR was developed for SRR channel estimation in the angular domain only.

Apart from using analog beamforming approach with phase only control to increase radar FoV, [12] used active phased array architecture with both phase and amplitude control, [13] proposed hybrid analog/digital architecture, and [14] proposed the mmWave multiple-input-multiple-output (MIMO) JCR technique. These approaches, however, have higher implementation complexity and power consumption than analog approaches using phased array architecture with phase only control. In [15], a practical fully-digital mmWave MIMO JCR solution was developed to achieve a high range and AoA estimation accuracy in a wide field of view. To realize the practical fully-digital mmWave MIMO JCR with low power consumption and hardware complexity, [15] proposed the use of 1-bit high-speed analog-to-digital converters per RF chain. The Cramér Rao bounds demonstrated that the MIMO JCR with 1-bit ADC performs closely to the infinite-bit ADC case for a single-target scenario at a low signal-to-noise ratio (SNR). The fully-digital mmWave MIMO solution with low-resolution ADCs, however, is not commercially available yet.

In this paper, we develop an adaptive combined waveform-beamforming design for mmWave automotive JCR that exploits all the TX antennas during the data transmission mode to perform a highly accurate SRR/MRR Doppler-angle domain channel estimation, at the cost of a small reduction in the communication data rate. We assume that the location and relative velocity of a target remain constant during a coherent processing interval (CPI). This assumption is justified by the small enough acceleration and velocity of a target relative to the radar sensor within a few milliseconds of CPI [16, Ch. 2], as found in automotive applications [1], [8], [10], [17]. We also assume full-duplex radar operation due to the recent development of systems with sufficient isolation and self-interference cancellation [18]. Additionally, we assume that the target range is in the far-field limit associated with the antenna array. In scenarios where the target range is below this limit, our solution can still be applied by turning off antenna elements to reduce the effective array aperture and decrease the far-field limit. Lastly, we assume perfect cancellation of the data part on the received training signal because the data is known at the transmitter, similar to [19]. This assumption is also motivated by the recent work on non-orthogonal multiple access techniques with successive interference cancellation [20]. Developing and evaluating algorithms to cancel the communication data interference with known data part while receiving the radar echoes is a subject of future work. The main contributions of this paper are summarized as follows:

- We propose a novel formulation for a mmWave automotive JCR system that performs automotive MRR and SRR sensing in a wide FoV without reducing the communication data rate much. This formulation captures the nuances of the sparse mmWave JCR channel with multiple targets in the Doppler-angle domain. Our proposed JCR system employs a generic TX waveform structure and uses a tunable TX beamforming design that can be optimized to achieve enhanced JCR performance using sparse sensing techniques.
- We develop a convolutional CS (CCS)-JCR technique to estimate the 2D-radar channel in the Doppler-angle domain. In this technique, the transmitter applies circulant shifts of the JCR TX beamformer to acquire CS measurements at the radar receiver. We transform our CS problem into a partial Fourier CS problem in 2D [21]. We show that the space-time sensing constraints in our problem allows only fewer configurations of the subsampling locations than a general 2D partial Fourier CS problem of comparable dimensions.
- We propose an optimized CCS (OCCS)-JCR approach by carefully designing the circulant shifts applied at the transmitter for superior Doppler-angle domain channel reconstruction. The optimized circulant shifts result in a space-time sampling pattern that achieves minimum coherence in partial Fourier CS under the space-time sensing constraints of our developed JCR system model.

- We investigate the JCR performance trade-off using the normalized MSE (NMSE) metric for radar and a comparable distortion MSE (DMSE) metric for communication using analysis and simulations. Additionally, we formulate a MSE-based weighted average optimization problem for an adaptive combined waveform-beamforming mmWave JCR design in automotive applications that meets the Pareto-optimal bound. We solve the MSE-based optimization problem for our proposed OCCS-JCR approach in different target scenarios.
- Numerical results demonstrate that the proposed OCCS-JCR combined waveform and beamforming design estimates the MRR and SRR radar channel in the Doppler-angle domain with low NMSE, at the cost of small reduction in the communication DMSE. The proposed OCCS-JCR performs the best, followed by the random CCS (RCCS)-JCR that uses random circulant shifts, and the RS-JCR extended for the Doppler-angle domain radar channel estimation performs the worst.

The work in this paper is a significant extension of our submitted conference papers [11], [22]. In addition to the detailed exposition, we have included Doppler effect in the CCS-JCR system model, developed an adaptive combined waveform-beamforming design and a MSE-based weighted average optimized JCR design. The Doppler effect in our model introduces new constraints on the space-time sampling pattern in CCS which have not been studied in the CCS literature [22]–[24]. The CCS methods in [22]–[24] focus on the spatial or temporal dimensions, and do not optimize the sampling pattern for sparse recovery. In this paper, we optimize the space-time sampling pattern in CCS for joint Doppler-angle estimation and demonstrate the performance of our method using numerical results.

The rest of this paper is organized as follows. We formulate a JCR system model with a generic TX waveform structure and beamformer design algorithm in Section II. In Section III, we describe the CCS algorithm to estimate the radar channel in the Doppler-angle domain. Then, we outline the space-time sampling pattern optimization for the CCS-JCR in Section IV. In Section V, we describe the performance metrics and adaptive combined-waveform beamforming design for the proposed CCS-JCR. We present the numerical results in Section VI. Finally, we conclude our work and provide direction for future work in Section VII.

Notation: The operators $(\cdot)^*$ stands for conjugate transpose and $(\cdot)^{\mathrm{T}}$ for transpose of a matrix or a vector. $\mathcal{N}(\mu, \sigma^2)$ is used for a complex circularly symmetric Gaussian random variable with mean μ and variance σ^2. The set of integers is represented by $\mathbb{Z}$, the set of real numbers is represented by $\mathbb{R}$, and the set of complex numbers is denoted by $\mathbb{C}$. For a vector $\mathbf{a}$, $\mathbf{a}^k$ is a vector in which every entry of $\mathbf{a}$ is raised to the power of k. The ℓ_2 norm of $\mathbf{a}$ is $\|\mathbf{a}\|$. The m^{th} row and the m^{th} column of $\mathbf{A}$ are $\mathbf{A}(m,:)$ and $\mathbf{A}(:,m)$. $|\mathbf{A}|$ is a matrix that contains the entry-wise magnitudes of $\mathbf{A}$. $\mathbf{A} \odot \mathbf{B}$ is defined as the element-wise multiplication of $\mathbf{A}$ and $\mathbf{B}$ and the symbol $\circledast$ denotes the 2D-circular convolution operation. We use $\mathbf{e}_{m,M} \in \mathbb{R}^M$ to represent the m^{th} standard basis vector in the Euclidean space of real numbers with $\mathbf{e}_{m,M}^{\mathrm{T}} = [0, \ldots, 1, \ldots, 0]$, where 1 is at the $(m+1)^{\mathrm{th}}$ place. We use $\mathrm{phase}_b(x)$ to denote the b-bit phase quantized version of x. The matrix $\mathbf{U}_N \in \mathbb{C}^{N \times N}$ denotes the unitary Discrete Fourier Transform (DFT) matrix. Frequently used symbols in the paper are summarized in Table I and commonly used acronyms is summarized in Table II.

TABLE I
FREQUENTLY USED SYMBOLS

Notation	Description
T_{s}	Symbol period
T	CPI duration
M	Number of frames in a CPI
N	Number of elements in TX/RX antenna array
K	Number of target scattering centers in a given range bin
λ	carrier wavelength
W	Bandwidth
ρ	Number of building blocks of size L_{BLK} in a preamble
L_{r}	Number of symbols in a preamble with $L_{\mathrm{r}} = \rho L_{\mathrm{BLK}}$
δ	Fraction of TX power in the communication RX direction

TABLE II
FREQUENTLY USED ABBREVIATIONS

Abbreviation	Description
JCR	Joint communication-radar
SRR	Short-range radar
MRR	Medium-range radar
LRR	Long-range radar
MSE	Mean square error
NMSE	Normalized MSE
DMSE	Distortion MSE
CPI	Coherent processing interval
FoV	Field of view
TX	Transmit
RX	Receive
ZC	Zadoff-Chu
CCS	Convolutional compressed sensing
RS-JCR	Random switching-JCR approach
RCCS-JCR	Random CCS-JCR approach
OCCS-JCR	Optimized CCS-JCR approach

II. SYSTEM MODEL

We consider the use case where a source vehicle sends a mmWave JCR waveform to communicate with a recipient vehicle at a distance d_{c} moving with a relative velocity v_{c}, while simultaneously using the received echoes for automotive radar sensing, as shown in Fig. 1. We consider closely separated TX antenna array and RX antenna array mounted on both source and recipient vehicles. For simplicity, we assume that the antenna arrays are uniform linear arrays (ULAs) with N-elements each. We assume a phased array architecture with b-bit phase shifters at the TX and the RX, where the phase shift alphabet is

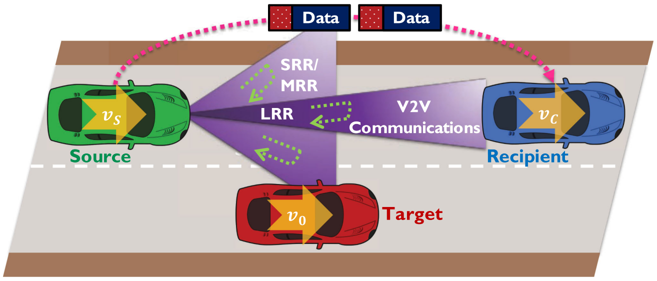

Fig. 1. An illustration of an automotive mmWave JCR system that simultaneously perform SRR/MRR radar sensing with a wide FoV and V2V communication with a narrow FoV.

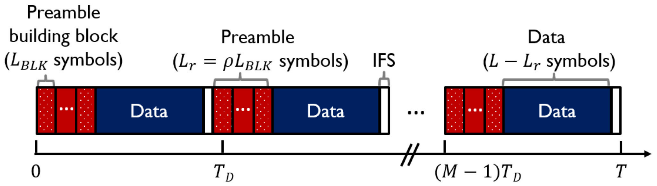

Fig. 2. A CPI of T seconds duration with M JCR equi-spaced frames separated by an IFS of $T_{\rm IFS}$. Each L-symbols frame consists of $L_{\rm r} = \rho L_{\rm BLK}$ number of preamble symbols and $(L - L_{\rm r})$ number of communication data symbols. Each frame is placed at an integer multiple of $T_{\rm D}$.

defined as $\mathbb{A}_b = \{e^{{\rm j}2n\pi/2^b}/\sqrt{N} : n \in \{0, 2, 3, \cdots 2^b - 1\}\}$. We assume the JCR transmitter generates a narrow beam towards the communication receiver without any blockage and distributes the remaining energy uniformly across the other directions for radar sensing.

A. Waveform Design for JCR

We consider a generic TX waveform structure with M equi-spaced frames separated by an inter-frame space (IFS) of $T_{\rm IFS}$ during a CPI of T seconds. Each L-symbols frame consists of a $L_{\rm r}$-symbols preamble part and $(L - L_{\rm r})$-symbols communication data segment, as shown in Fig. 2. We assume that the training sequences possess good correlation properties for communication channel estimation. We also assume that the training sequence length is an integer multiple ρ of the building block size $L_{\rm BLK}$, satisfying $L_{\rm r} = \rho L_{\rm BLK}$. Golay sequences can be used to construct this preamble structure with arbitrary ρ and preamble length $\rho L_{\rm BLK}$, where the binary logarithm of $L_{\rm BLK}$ is an integer [3]. Similar to [8], we exploit the training sequences used in the preamble with good properties for radar sensing.

The mmWave WLAN standard [3] with Golay complementary sequences can realize the proposed JCR frame structure. Additionally, the IEEE 802.11ad standard can realize this multi-frame approach using the block/no acknowledgment policy during the communication between a dedicated pair of nodes in the data transmission interval [3, Ch. 9]. The communication receiver can estimate the training sequence length by designing a symbol boundary detection algorithm that detects when the preamble ends. This can be implemented similar to the one currently employed for symbol boundary detection algorithm in IEEE 802.11ad standard by placing a special Golay sequence of length 128 at the end of the short training field [25]. The exact implementation of preamble length detection technique at the communication receiver is left for future work.

To unambiguously estimate a maximum relative target velocity $v_{\max}$ in a CPI, the $m^{\rm th}$ frame is considered to be located at an integer multiple, m, of the Doppler Nyquist sampling interval $T_{\rm D}$. Here, $T_{\rm D} \leq \lambda/(4v_{\max})$ where λ is the wavelength. To enhance the radar estimation performance of the mmWave JCR without decreasing communication rate much, we propose to optimize ρ and thereby the length of the training sequence. The analysis in this paper can be extended to a virtual waveform design structure with non-uniformly placed frames similar to [19].

We denote the unit energy TX pulse-shaping filter as $g_{\rm t}(t)$, the signaling bandwidth as W, and the symbol period as $T_{\rm s} \approx 1/W$. The $\ell^{\rm th}$ TX symbol corresponding to the $m^{\rm th}$ frame is denoted by $s_{m,\ell}[\rho]$, which is a function of the tunable preamble length parameter ρ. The TX symbol satisfies the average power constraint $\mathbb{E}[|s_{m,\ell}[\rho]|^2] = \mathcal{E}_{\rm s}$. Then, the generic complex-baseband continuous-time representation of the single-carrier TX waveform in a CPI is given as

$$x(t, \rho) = \sum_{m=0}^{M-1} \sum_{\ell=0}^{L-1} s_{m,\ell}[\rho] g_{\rm t}(t - \ell T_{\rm s} - mT_{\rm D}), \tag{1}$$

where $L = (T_{\rm D} - T_{\rm IFS})/T_{\rm s}$.

B. Beamformer Design for JCR

In this subsection, we explain our approach to construct a collection of beamformers that are well suited to the automotive JCR application. Our method first constructs one sequence for each of the TX and RX. These sequences are designed according to the JCR specification. In this specification, a good JCR beamformer is one that has a reasonable gain along the communication direction and sufficient power along the sensing directions for radar. The use of a single JCR beamformer, however, may not be sufficient to detect multiple targets. To this end, our method constructs a collection of beamformers by circularly shifting the beamformers constructed at the TX and the RX. As circulant shifts of a vector preserve the magnitude of its DFT, the proposed method ensures that the beams constructed according to our procedure achieve the desired JCR specification. The collection of circularly shifted beamformers is used to acquire distinct radar channel measurements.

During a CPI, our JCR design uses an adaptive collection of TX and RX beams to achieve a high-resolution radar sensing in a wide FoV with a minimal reduction in the communication data rate. We would like to highlight that a wide FoV is a requirement for SRR and MRR automotive radars [1], [26]. Additionally, the use of wide FoV will enable radars to see additional targets that are in a different direction than the communication receivers. Due to the use of wide FoV and high two-way radar channel path-loss, we focus on short-range and medium-range automotive radar scenarios for the proposed JCR combined waveform-beamforming design. This work can be extended to long-range automotive radar by decreasing the field of view for radars. We propose to use δ fraction of TX power along the communication receiver direction, θ_0, and $1 - \delta$ fraction of TX power along the

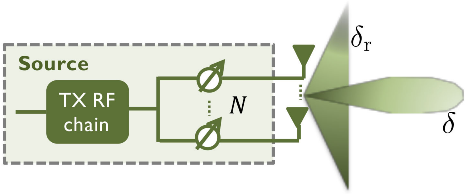

(a) JCR TX beamforming at the source vehicle

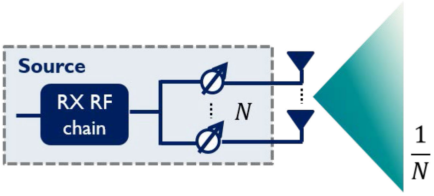

(b) Radar RX beamforming at the source vehicle

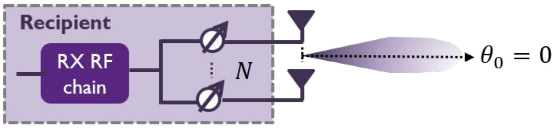

(c) Communication RX beamforming at the recipient vehicle

Fig. 3. The JCR TX ULA at the source vehicle in (a) generates a narrow coherent beam for communication and distributes the remaining energy uniformly along the other directions for radar sensing. Here, the communication angle $\theta_0 = 0$. The radar RX ULA at the source vehicle in (b) forms a $1/N$ constant gain beam for radar sensing, while the communication RX ULA at the recipient vehicle in (c) generates a narrow coherent beam pointed towards the JCR source transmitter.

other directions for radar sensing. Within a CPI, the transmitter applies M different beamforming vectors to acquire distinct radar channel measurements. The source vehicle uses M unit norm TX beamforming vectors $\{\mathbf{f}_m(\delta)\}_{m=0}^{M-1}$. Therefore, the TX signal at the source vehicle during a CPI is

$$\mathbf{x}_{\mathrm{t}}(t,\rho) = \mathbf{f}_m(\delta)x(t,\rho), \quad 0 \leq t \leq T. \tag{2}$$

To enhance the radar estimation performance of the mmWave JCR without decreasing communication rate much, we also propose to optimize δ under a per-antenna power constraint.

We explain the key idea underlying the proposed TX beamformer design technique. For tractability, we design the beamformer by considering a DFT grid with N discrete angles. For ease of exposition, we assume the communication direction is 0°. The JCR TX beamformer design problem is to design a sequence $\mathbf{f}_{\mathrm{t}}(\delta) \in {\mathbb{A}_b}^N$ whose beampattern has an energy of δ along 0°. The remaining energy in the beamformer must be distributed across the other directions to enable radar channel reconstruction from sub-Nyquist channel measurements. Prior work has shown that beamformers with close to uniform gain along the desired sensing directions enable fast CS channel reconstruction [23]. To this end, the proposed construction distributes the energy of $1-\delta$ "uniformly" across the remaining DFT grid locations, as shown in Fig. 3.

We use the Gerchberg Saxton (GS) algorithm [27] to construct the desired JCR beamformer at the TX [See Algorithm 1]. By the JCR specification, we seek an $\mathbf{f}_{\mathrm{t}}(\delta)$ whose discrete beam pattern has an energy of δ along 0° and $\delta_r = (1-\delta)/(N-1)$ along the remaining $N-1$ directions. The discrete beam pattern is simply the N-point DFT of the vector $\mathbf{f}_{\mathrm{t}}(\delta)$. Therefore, the DFT magnitude vector associated with the desired beamformer is

$$\tilde{\mathbf{f}}_{\mathrm{mag}}(\delta) = [\sqrt{\delta}, \sqrt{\delta_{\mathrm{r}}}, \sqrt{\delta_{\mathrm{r}}}, \ldots, \sqrt{\delta_{\mathrm{r}}}]^{\mathrm{T}}. \tag{3}$$

A naive approach to construct the desired JCR beamformer is to apply an inverse DFT over $\tilde{\mathbf{f}}_{\mathrm{mag}}(\delta)$. The inverse DFT of $\tilde{\mathbf{f}}_{\mathrm{mag}}(\delta)$, however, may not be an element in ${\mathbb{A}_b}^N$. The GS algorithm is an alternating projection method that finds a sequence in ${\mathbb{A}_b}^N$ such that the magnitude of its DFT is close to $\tilde{\mathbf{f}}_{\mathrm{mag}}(\delta)$. We initialize $\mathbf{f}_{\mathrm{t}}(\delta)$ to a Zadoff-Chu (ZC) sequence that has a quasi-omnidirectional beam pattern. We observed that such an initialization results in a better JCR beamformer when compared to using sequences which have a directional beam pattern.

Algorithm 1: GS algorithm to find $\mathbf{f}_{\mathrm{t}}(\delta)$.

```
Inputs: $\delta$, $N$, $b$, $T_{\mathrm{GS}}$, and $\tilde{\mathbf{f}}_{\mathrm{mag}}(\delta)$.
Initialize: Set $t_{\mathrm{iter}} = 1$ and $\mathbf{f}_{\mathrm{t}}(\delta)$ to a ZC sequence.
while $t_{\mathrm{iter}} < T_{\mathrm{GS}}$ do
    $\tilde{\mathbf{f}}_{\mathrm{phase}}(\delta) \leftarrow \mathrm{phase}(\mathrm{DFT}(\mathbf{f}_{\mathrm{t}}(\delta)))$
    Constraint on the discrete beam pattern:
    $\tilde{\mathbf{f}}(\delta) \leftarrow \tilde{\mathbf{f}}_{\mathrm{mag}}(\delta) \odot \exp(\mathrm{j}\tilde{\mathbf{f}}_{\mathrm{phase}}(\delta))$
    Constraint on the antenna weights:
    $\mathbf{f}_{\mathrm{phase}}(\delta) \leftarrow \mathrm{phase}_b(\mathrm{IDFT}(\tilde{\mathbf{f}}(\delta)))$
    $\mathbf{f}_{\mathrm{t}}(\delta) \leftarrow \exp(\mathrm{j}\mathbf{f}_{\mathrm{phase}}(\delta))/\sqrt{N}$
end while
return $\mathbf{f}_{\mathrm{t}}(\delta)$.
```

The proposed GS-based beamformer design procedure can be generalized for any communication direction $\theta \neq 0^o$. For an N-element ULA with elements half-wavelength spaced, we define the array steering vector $\mathbf{a}(\theta) \in \mathbb{C}^N$ with far-field assumption as

$$\mathbf{a}(\theta) = \left[1, e^{\mathrm{j}\pi\sin\theta}, e^{\mathrm{j}2\pi\sin\theta}, \ldots, e^{\mathrm{j}(N-1)\pi\sin\theta}\right]^{\mathrm{T}}. \tag{4}$$

The TX beamformer in such a case is defined as $\mathbf{f}_{\mathrm{t}}(\delta) \odot \mathbf{a}(\theta)$. For large antenna arrays at very short ranges, however, the near-field effect starts to dominate. In such a case, it is possible to split the antenna array into several sub-sections where the far-field approximation can be applied [28]. Then, the proposed JCR design can be applied to each of these sub-sections to acquire radar measurements. Finally, a message passing-based algorithm can be used to exploit the structure within and across the sparse channels associated with the different sub-sections [28], [29]. In this paper, however, we make the far-field assumption to obtain the radar channel. Extending our method to near field settings is beyond the scope of this paper and is left for future work.

In our design, every JCR beamformer $\mathbf{f}_m(\delta)$ is constructed by circulantly shifting $\mathbf{f}_{\mathrm{t}}(\delta)$. As circulantly shifting a vector preserves the magnitude of its DFT, $\mathbf{f}_m(\delta)$ has the same discrete beam pattern as $\mathbf{f}_{\mathrm{t}}(\delta)$. Therefore, the vectors $\{\mathbf{f}_m(\delta)\}_{m=0}^{M-1}$ satisfy the desired JCR specification. The TX beam pattern achieved by the GS algorithm for $N = 256$ and its comparison with RS-based JCR as well as ideal communications are illustrated in our paper [22].

The receiver at the source vehicle uses a unit norm RX beamforming vector $\mathbf{f}_{\mathrm{r}}$. We propose to set the RX combiner vector $\mathbf{f}_{\mathrm{r}}$ to a ZC sequence in ${\mathbb{A}_b}^N$. Such a vector results in quasi-omnidirectional reception at the radar receiver, which enables radar scanning mode with no prior knowledge of radar target directions. We would like to highlight that the combiner vector at the RX is fixed throughout the radar channel measurement process. The fixed quasi-omnidirectional receive beam allows us to drop the AoA estimation problem in our measurement model, and focus on joint AoD-Doppler estimation. Extending our method to joint AoA, AoD, and Doppler estimation in radar tracking mode is an interesting direction for future work.

The communication receiver of the recipient vehicle uses a unit norm beamforming vector defined as $\mathbf{f}_{\mathrm{c}}$. This beamformer $\mathbf{f}_{\mathrm{c}}$ is set to a spatial matched filter of the communication channel to provide the maximum TX-RX array gain and thereby achieve the highest communication spectral efficiency.

C. Received Signal Model

Within a CPI of T seconds, we assume that the acceleration and the relative velocity of a moving target is small enough to assume constant velocity and that the target is quasi-stationary (constant location parameters). We represent the SRR/MRR radar channel as a doubly selective mmWave channel [1]. Due to the one-way channel used in communications as compared to the two-way channel used in radars, the delay spread of communication channels is smaller than the radar channels. The delay spread for communication channel further reduces due to the narrow mainlobe pointing towards the communication receiver at a long distance [30], as compared to the wide sidelobe used for radar sensing at short or medium ranges [1]. Therefore, to explore the performance trade-off between communication and radar, we consider an illustrative example of a line-of-sight, frequency-flat mmWave communication channel between the source and recipient vehicles [8], [11], [30]. Nonetheless, the approach developed in this paper can be extended for different scattering scenarios by including frequency-selective communication channels; the extension is omitted because of space limitations. After the RX matched filtering, and symbol rate sampling, the communication/radar RX signal model in a CPI can be formulated as follows.

Communication received signal model: We assume that the channel is time-invariant during a single frame because the relative velocity between the source and target vehicles are small. We do not include band-limited filters in the channel model and instead include them in the TX/RX signal models. The communication channel between the source and recipient vehicle is characterized by its complex channel amplitude h_{c}, angle-of-departure (AoD) and AoA pair (θ_0, ϕ_0), path delay d_{c}/c with c being the speed of light.

Assuming perfect synchronization and additive noise $w_{\mathrm{c},m,\ell} \sim \mathcal{N}(0, \sigma_{\mathrm{c}}^2)$, the received communication signal with the TX steering vector $\mathbf{a}(\theta_0)$, the RX steering vector $\mathbf{a}(\phi_0)$, and the channel $\mathbf{H}_{\mathrm{c}} = h_{\mathrm{c}} \mathbf{a}(\phi_0) \mathbf{a}^*(\theta_0)$ is

$$y_{\mathrm{c},m,\ell}(\rho, \delta) = \mathbf{f}_{\mathrm{c}}^* \mathbf{H}_{\mathrm{c}} \mathbf{f}_m(\delta) s_{m,\ell}[\rho] + w_{\mathrm{c},m,\ell}. \tag{5}$$

Assuming that the TX and RX beams are perfectly aligned and directional beamforming with a spatial matched filter is used at the RX to provide the maximum TX-RX array gain for the considered line-of-sight channel model, (5) simplifies as

$$y_{\mathrm{c},m,\ell}(\rho, \delta) = \sqrt{\delta} N h_{\mathrm{c}} s_{m,\ell}[\rho] + w_{\mathrm{c},m,\ell}. \tag{6}$$

We define communication signal-to-noise ratio (SNR) corresponding to the ideal beampattern for communication with $\delta = 1$ as $\zeta_{\mathrm{c}} = \mathcal{E}_{\mathrm{s}} |h_{\mathrm{c}}|^2 \, N^2 / {\sigma_{\mathrm{c}}}^2$. In this case, the net received signal SNR increases linearly with the fraction of TX power for communication and is given by $\delta \zeta_{\mathrm{c}}$.

Radar received signal model: We represent the doubly selective (time- and frequency-selective) mmWave radar channel using virtual representation obtained by uniform sampling in range, Doppler, and AoD dimensions [8]. The range estimation is assumed to be performed before Doppler and angle estimation using correlation processing as in other references [8], [19]. Since the focus of this paper is target detection/estimation in the Doppler-AoD domain and not in the range domain, we describe radar signal model for a particular dominant range bin with distance d [11]. The same algorithm can be applied to the other range bins. The insights and analysis developed in this paper can be extended to other range bins.

We assume that the range bin of interest consists of a few, K, virtual target scattering centers. Here, $K < N$. The k^{th} virtual scattering center is described by its Doppler-AoD pair (ν_k, θ_k) and complex channel amplitude h_k, which is a product of radar cross-section and path-loss. After the RX beamfoming, after the cross-correlation of the TX training sequences with the m^{th} received frame echo, and assuming perfect cancellation of the data part on the received training signal [19], the radar received signal corresponding to the training part with an additive noise $w_m[\rho]$ is given as

$$y_m(\rho, \delta) = \sum_{k=0}^{K-1} h_k \mathrm{e}^{-\mathrm{j}2\pi \nu_k m T_{\mathrm{D}}} \mathbf{a}^*(\theta_k) \mathbf{f}_m(\delta) + w_m[\rho]. \tag{7}$$

We assume the thermal noise in the receiver is an additive white Gaussian noise with variance σ^2. We denote $\gamma[\rho]$ as the product of the RX beamforming gain and the integration gain due to the employed cross-correlation, which depends on the training sequence length used within a frame. Then, the additive noise $w_m[\rho]$ corresponding to the m^{th} frame in (7) is distributed as $\mathcal{N}(0, \sigma^2 / \mathcal{E}_{\mathrm{s}} \gamma[\rho])$.

We denote the Doppler shift vector $\mathbf{d}(\nu_k)$ as

$$\mathbf{d}(\nu_k) = \left[1, \mathrm{e}^{-\mathrm{j}2\pi \nu_k T_{\mathrm{D}}}, \ldots, \mathrm{e}^{-\mathrm{j}2\pi \nu_k (M-1) T_{\mathrm{D}}}\right]^{\mathrm{T}}. \tag{8}$$

We represent the radar channel in a CPI be expressed as

$$\mathbf{H} = \sum_{k=0}^{K-1} h_k \mathbf{d}(v_k) \mathbf{a}^*(\theta_k). \tag{9}$$

We observe that $\mathrm{e}^{-\mathrm{j}2\pi\nu_k m T_{\mathrm{D}}}$ in (7) can be expressed as $\mathbf{e}_{m,M}^{\mathrm{T}}\mathbf{d}(\nu_k)$. Putting this observation in (7) and using the definition of $\mathbf{H}$, we can write

$$y_m(\rho,\delta)=\mathbf{e}_{m,M}^{\mathrm{T}}\mathbf{H}\mathbf{f}_m(\delta)+w_m[\rho]. \tag{10}$$

We define the SNR of the received radar signal excluding the preamble correlation gain and the TX beamforming gain as $\zeta=\mathcal{E}_{\mathrm{s}}\beta\gamma[0]/\sigma^2$ with average target channel power β. We denote the SNR that includes the preamble correlation gain but excludes the TX beamforming gain as $\zeta_{\mathrm{p}}[\rho]=\mathcal{E}_{\mathrm{s}}\beta\gamma[\rho]/\sigma^2$.

III. CONVOLUTIONAL CS IN A RADAR SETTING

The radar channel $\mathbf{H}\in\mathbb{C}^{M\times N}$ encodes the Doppler shift and AoD information of the targets. Due to the propagation characteristics of the environment at mmWave frequencies, the channel is approximately sparse when expressed in an appropriate basis [31]. For instance, the 2D-DFT basis is often chosen for the sparse representation of $\mathbf{H}$ [32]. Let $\tilde{\mathbf{H}}\in\mathbb{C}^{M\times N}$ denote the inverse 2D-DFT of $\mathbf{H}$ such that

$$\mathbf{H}=\mathbf{U}_M\tilde{\mathbf{H}}\mathbf{U}_N. \tag{11}$$

Equivalently, $\tilde{\mathbf{H}}=\mathbf{U}_M^{*}\mathbf{H}\mathbf{U}_N^{*}$.[1] The matrix $\mathbf{H}$ is the time-antenna domain channel and $\tilde{\mathbf{H}}$ is called as the Doppler-angle domain channel. The sparse structure in $\tilde{\mathbf{H}}$ at mmWave allows the use of CS techniques to estimate $\tilde{\mathbf{H}}$ from sub-Nyquist radar channel measurements.

In this paper, we use a special class of CS called convolutional CS [24] for sparse radar channel estimation. In this technique, the TX applies circulant shifts of the JCR beamforming vector $\mathbf{f}_{\mathrm{t}}(\delta)$. We use $c[m]$ to denote the circulant shift used at the TX in the m^{th} measurement slot. Here, $c[m]$ is an integer in $\{0,1,\ldots,N-1\}$. The beamforming vector applied at the TX is then $\mathbf{f}_m(\delta)=\mathbf{J}_{c[m]}\mathbf{f}_{\mathrm{t}}(\delta)$, where $\mathbf{J}_{c[m]}\in\mathbb{R}^{N\times N}$ is the right circulant-delay matrix corresponding to a shift of $c[m]$ units. For example, $\mathbf{J}_1\in\mathbb{R}^{3\times 3}$ is

$$\mathbf{J}_1=\begin{bmatrix}0&1&0\\0&0&1\\1&0&0\end{bmatrix}. \tag{12}$$

In general, $\mathbf{J}_i=(\mathbf{J}_1)^i$. $\mathbf{J}_0$ is the $N\times N$ Identity matrix. We substitute the beamforming vector in (10) to write

$$y_m(\rho,\delta)=\mathbf{e}_{m,M}^{\mathrm{T}}\mathbf{U}_M\tilde{\mathbf{H}}\mathbf{U}_N\mathbf{J}_{c[m]}\mathbf{f}_{\mathrm{t}}(\delta)+w_m(\rho). \tag{13}$$

The convolutional structure in the beamforming weights used at the TX allows sparse recovery algorithms to exploit the fast Fourier transform [23].

We show that $y_m(\rho,\delta)$ in (13) can be interpreted as a 2D-DFT measurement of another sparse matrix called the masked Doppler-angle matrix. To define this matrix, we first simplify $\mathbf{U}_N\mathbf{J}_{c[m]}\mathbf{f}_{\mathrm{t}}(\delta)$ in (13). We define a diagonal matrix containing the scaled DFT of $\mathbf{f}_{\mathrm{t}}(\delta)$ on its diagonal as

$$\mathbf{\Lambda}(\delta)=\sqrt{N}\mathrm{diag}(\mathbf{U}_N\mathbf{f}_{\mathrm{t}}(\delta)). \tag{14}$$

By the property that circulantly shifting a vector modulates the phase of its DFT representation, the DFT of $\mathbf{f}_m(\delta)=\mathbf{J}_{c[m]}\mathbf{f}_{\mathrm{t}}(\delta)$ can be expressed as

$$\mathbf{U}_N\mathbf{J}_{c[m]}\mathbf{f}_{\mathrm{t}}(\delta)=\mathbf{\Lambda}(\delta)\mathbf{U}_N\mathbf{e}_{c[m],N}. \tag{15}$$

We define $\tilde{\mathbf{Z}}(\delta)=\tilde{\mathbf{H}}\mathbf{\Lambda}(\delta)$ as the masked Doppler-angle matrix. The mask is due to the multiplication effect induced by $\mathbf{\Lambda}(\delta)$ on the columns of $\tilde{\mathbf{H}}$. The matrix $\tilde{\mathbf{Z}}(\delta)$ is sparse as $\tilde{\mathbf{H}}$ is sparse and $\mathbf{\Lambda}(\delta)$ is diagonal. As all the diagonal entries in $\mathbf{\Lambda}(\delta)$ are non-zero with our design in Algorithm 1, information about all the targets is preserved in $\tilde{\mathbf{Z}}(\delta)$. The rows and columns of $\tilde{\mathbf{Z}}(\delta)$ correspond to the Doppler and the angle bins. In this paper, we focus on estimating the sparse matrix $\tilde{\mathbf{Z}}(\delta)$ instead of the sparse $\tilde{\mathbf{H}}$. Such an approach allows a tractable CS matrix design. Denoting $\mathbf{e}_{c[m],N}$ as a standard basis vector in $\mathbb{R}^N$, the measurement in (13) can be simplified using (15) as

$$y_m(\rho,\delta)=\mathbf{e}_{m,M}^{\mathrm{T}}\mathbf{U}_M\underbrace{\tilde{\mathbf{H}}\mathbf{\Lambda}(\delta)}_{\tilde{\mathbf{Z}}(\delta)}\mathbf{U}_N\mathbf{e}_{c[m],N}+w_m[\rho] \tag{16}$$

$$=\mathbf{e}_{m,M}^{\mathrm{T}}\underbrace{\mathbf{U}_M\tilde{\mathbf{Z}}(\delta)\mathbf{U}_N}_{\text{2D}-\text{DFT of }\tilde{\mathbf{Z}}(\delta)}\mathbf{e}_{c[m],N}+w_m[\rho]. \tag{17}$$

We observe from (17) that the m^{th} channel measurement with the circulant shift-based training is the $(m,c[m])^{\mathrm{th}}$ entry of the 2D-DFT of $\tilde{\mathbf{Z}}(\delta)$.

We explain sparse recovery of $\tilde{\mathbf{Z}}(\delta)$ using a partial 2D-DFT CS problem and explain the notion of a space-time trajectory. We observe from (17) that the RX acquires M radar channel measurements when the TX applies M circulant shifts of $\mathbf{f}_{\mathrm{t}}(\delta)$. The measurements in (17) are subsamples from an $M\times N$ matrix $\mathbf{Z}(\delta)$ which is defined as

$$\mathbf{Z}(\delta)=\mathbf{U}_M\tilde{\mathbf{Z}}(\delta)\mathbf{U}_N. \tag{18}$$

From (17) and (18), we notice that our approach obtains the entries of $\mathbf{Z}(\delta)$ at the 2D-coordinates $\{(m,c[m])\}_{m=0}^{M-1}$ on an $M\times N$ grid. A trajectory is defined as a 2D-path on this grid which traverses through $(m,c[m])_{m=0}^{M-1}$ in sequence. The row and column coordinates of the traversed locations, i.e., m and $c[m]$, correspond to the time and space dimensions. The space-time constraint in our problem is due to the fact that the column coordinate $c[m]$ is a function of the row coordinate m. We define the set of 2D coordinates as $\Omega=\{(0,c[0]),(1,c[1]),\ldots,(m,c[m]),\cdots(M-1,c[M-1])\}$. An example of a trajectory for $M=5$ and $N=5$ is shown in Fig. 4. Note that the trajectory goes through just one coordinate on the 2D-grid for each time slot index m. As the goal is to estimate the sparse matrix $\tilde{\mathbf{Z}}(\delta)$ from the subsamples of its 2D-DFT $\mathbf{Z}(\delta)$, the sparse recovery problem is a partial 2D-DFT CS problem [21].

The reconstruction performance with partial 2D-DFT CS depends on the subsampling trajectory. Prior work has shown that fully random subsampling trajectories can achieve sparse recovery with partial 2D-DFT CS [33]. Trajectories that are fully random over an $M\times N$ grid, however, cannot be used in the sparse Doppler-angle estimation problem due to the space-time sampling constraint in our problem. For example, a

---

[1] The usual convention in radar is that the Doppler-angle channel is the Fourier transform of the time-antenna channel. In this paper, we use the inverse Fourier transform for ease of notation.

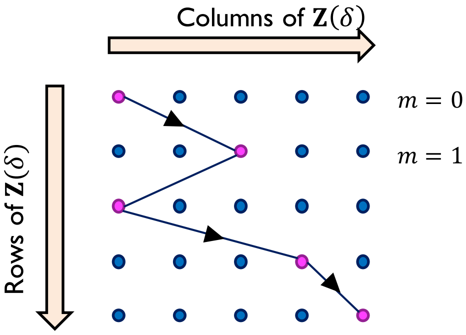

Fig. 4. The sampling trajectory traverses through just one element in every row of $\mathbf{Z}(\delta)$ for the combined-waveform beamforming design in the CCS-JCR approach.

2D-trajectory cannot go through (0,0) and (0,1) as Ω must have a single 2D-coordinate with $m = 0$. Therefore, the number of feasible 2D-trajectories in our problem is smaller when compared to a typical partial 2D-DFT CS problem where the trajectories traverse through a 2D-spatial grid. The space-time nature of the 2D-CS problem in this work complicates the trajectory design problem.

The number of feasible trajectories under the space-time sampling constraint is N^M. This is because there are N possible circulant shifts for $c[m] \forall m$. A reasonable choice for the subsampling trajectory is one that is chosen at random from the N^M feasible candidates. In Section IV, we propose a novel deterministic subsampling trajectory that achieves better channel reconstruction than a feasible random trajectory.

IV. SPACE-TIME SUBSAMPLING TRAJECTORY DESIGN

A good subsampling trajectory is one that results in a CS matrix with the smallest coherence [34]. This is because a lower coherence results in better sparse recovery [34]. In this section, we give an explicit form of the CS matrix and derive the desired space-time subsampling trajectory.

We use $\mathbf{A} \in \mathbb{C}^{M \times MN}$ to denote the CS matrix corresponding to the partial 2D-DFT measurement model in (17). The m^{th} row of $\mathbf{A}$ is defined as

$$\mathbf{A}(m,:) = (\mathbf{e}^{\mathrm{T}}_{c[m],N}\mathbf{U}_N) \otimes (\mathbf{e}^{\mathrm{T}}_{m,M}\mathbf{U}_M). \tag{19}$$

We rewrite (17) with the radar noise vector $\mathbf{w}[\rho] = [w_0[\rho], w_1[\rho], \dots, w_{M-1}[\rho]]^{\mathrm{T}}$, the radar channel measurement vector $\mathbf{y}(\rho,\delta) = [y_0(\rho,\delta), y_1(\rho,\delta), \dots, y_{M-1}(\rho,\delta)]$, and the masked Doppler-angle matrix $\tilde{\mathbf{z}}(\delta) = \mathrm{vec}(\tilde{\mathbf{Z}}(\delta))$, as

$$\mathbf{y}(\rho,\delta) = \mathbf{A}\tilde{\mathbf{z}}(\delta) + \mathbf{w}[\rho], \tag{20}$$

which is the standard CS linear measurement model.

The coherence of the CS matrix $\mathbf{A}$ in (19) is defined as [34]

$$\mu = \max_{(i,\ell), i \neq \ell} \frac{|(\mathbf{A}(:,i))^{*}\mathbf{A}(:,\ell)|}{\|\mathbf{A}(:,i)\|\|\mathbf{A}(:,\ell)\|}. \tag{21}$$

Due to the partial 2D-DFT nature of $\mathbf{A}$, the coherence μ can also be expressed in terms of the point spread function (PSF) associated with the subsampling trajectory [35]. To explain the PSF, we first define an $M \times N$ binary subsampling matrix $\mathbf{B}$ where

$$\mathbf{B}(m,n) = \begin{cases} 1, & \text{if } (m,n) \in \Omega \\ 0, & \text{if } (m,n) \notin \Omega \end{cases}. \tag{22}$$

We define $\tilde{\mathbf{B}}$, the 2D-DFT of $\mathbf{B}$, as the PSF. Specifically, $\tilde{\mathbf{B}} = \mathbf{U}_M\mathbf{B}\mathbf{U}_N$. Now, μ in (21) can also be expressed as [35], [36]

$$\mu = \frac{\sqrt{MN}}{M} \max_{(p,q)\neq(0,0)} |\tilde{\mathbf{B}}(p,q)|. \tag{23}$$

The focus of this section is to construct the subsampling set $\Omega = \{(m, c[m])\}_{m=0}^{M-1}$ that results in the smallest μ under the sampling constraints in our problem.

We now discuss the structure of the PSF $\tilde{\mathbf{B}}$ under the sampling constraints. We observe from (22) that the m^{th} row of $\mathbf{B}$ has a single one in the $c[m]^{\text{th}}$ column and has zeros at the other locations for $\Omega = \{(m, c[m])\}_{m=0}^{M-1}$. The $M \times N$ binary subsampling matrix is

$$\mathbf{B} = \begin{pmatrix} \mathbf{e}^{T}_{c[0],N} \\ \mathbf{e}^{T}_{c[1],N} \\ \vdots \\ \mathbf{e}^{T}_{c[M-1],N} \end{pmatrix}. \tag{24}$$

We define $\omega = \exp(-\mathrm{j}2\pi/N)$ and compute the PSF $\tilde{\mathbf{B}}$ from $\mathbf{B}$ in (24). First, we find the N-point DFT of every row in $\mathbf{B}$. Since $\mathbf{e}^{T}_{c[m],N}\mathbf{U}_N = [1, \omega^{c[m]}, \omega^{2c[m]}, \dots, \omega^{(N-1)c[m]}]/\sqrt{N}$, we can write

$$\mathbf{B}\mathbf{U}_N = \frac{1}{\sqrt{N}} \begin{bmatrix} 1 & \omega^{c[0]} & \omega^{2c[0]} & \dots & \omega^{(N-1)c[0]} \\ 1 & \omega^{c[1]} & \omega^{2c[1]} & \dots & \omega^{(N-1)c[1]} \\ \vdots & \vdots & \vdots & & \vdots \\ 1 & \omega^{c[M-1]} & \omega^{2c[M-1]} & \dots & \omega^{(N-1)c[M-1]} \end{bmatrix}. \tag{25}$$

To express (25) in compact form, we define $\mathbf{g} \in \mathbb{C}^M$ as

$$\mathbf{g} = [\omega^{c[0]}, \omega^{c[1]}, \dots, \omega^{c[M-1]}]^T. \tag{26}$$

Then,

$$\mathbf{B}\mathbf{U}_N = [\mathbf{g}^0, \mathbf{g}^1, \mathbf{g}^2, \dots, \mathbf{g}^{N-1}]/\sqrt{N}. \tag{27}$$

Note that $\mathbf{g}^0 = \mathbf{1}$, where $\mathbf{1}$ is an all-ones vector of length M. Now, the PSF $\tilde{\mathbf{B}} = \mathbf{U}_M\mathbf{B}\mathbf{U}_N$ is obtained by taking the M-point DFT of every column in $\mathbf{B}\mathbf{U}_N$, i.e.,

$$\tilde{\mathbf{B}} = [\mathbf{U}_M\mathbf{g}^0, \mathbf{U}_M\mathbf{g}^1, \mathbf{U}_M\mathbf{g}^2, \dots, \mathbf{U}_M\mathbf{g}^{N-1}]/\sqrt{N}. \tag{28}$$

The problem now is to find a vector $\mathbf{g}$ of the form in (26) such that the PSF in (28) achieves the smallest coherence.

We now examine the entries of the PSF. The first column of $\tilde{\mathbf{B}}$ in (28) is the DFT of $\mathbf{1}/\sqrt{N}$, which is the M length vector $\sqrt{M/N}\mathbf{e}_{0,M}$. As all the entries in the first column other than $\tilde{\mathbf{B}}(0,0)$ are 0, this column does not impact μ defined in (23). The other columns of $\tilde{\mathbf{B}}$ which have the form $\mathbf{U}_M\mathbf{g}^q$ for $q \neq 0$ determine μ. To achieve the smallest coherence, the largest entry of $|\mathbf{U}_M\mathbf{g}^q|$ must be minimized for every $q \in \{1, 2, 3, \dots, N-1\}$. As $\|\mathbf{g}^q\| = \sqrt{M}$, it follows that $\|\mathbf{U}_M\mathbf{g}^q\| = \sqrt{M}$ for every q. Under this norm constraint, the largest entry of $|\mathbf{U}_M\mathbf{g}^q|$ can be no smaller than 1. Therefore, we seek a $\mathbf{g}$ such that

$$|\mathbf{U}_M \mathbf{g}^q| = \mathbf{1},\ \forall q \in \{1, 2, 3, \ldots, N-1\}, \tag{29}$$

i.e., the DFT of every q^{th} power of $\mathbf{g}$ must have a constant magnitude for $1 \leq q \leq N-1$. Furthermore, $\mathbf{g}$ must be expressible in the form of (26).

We discuss why the ZC sequence is a reasonable choice for the vector $\mathbf{g}$. We use $\boldsymbol{\xi} \in \mathbb{C}^M$ to denote a ZC sequence of root u and length M. Here, u is co-prime with M. The m^{th} entry of $\boldsymbol{\xi}$ is [37]

$$\xi[m] = \begin{cases} \exp\left(-\mathrm{j}\frac{\pi u m(m+1)}{M}\right), & \text{if } M \text{ is odd} \\ \exp\left(-\mathrm{j}\frac{\pi u m^2}{M}\right), & \text{if } M \text{ is even} \end{cases}. \tag{30}$$

An interesting property is that the DFT of a ZC sequence has a constant magnitude, i.e., $|\mathbf{U}_M \boldsymbol{\xi}| = \mathbf{1}$ [38]. When $\mathbf{g}$ is set to $\boldsymbol{\xi}$, we observe that the unimodular DFT condition in (29) holds when $q = 1$. Now, we notice from (30) that $\mathbf{g}^q = \boldsymbol{\xi}^q$ has the same structure as $\boldsymbol{\xi}$, but with root qu instead of u. When qu is coprime with M, $\mathbf{g}^q$ is a ZC sequence that satisfies $|\mathbf{U}_M \mathbf{g}^q| = \mathbf{1}$. Therefore, the condition in (29) is met when $\mathbf{g}$ is a ZC sequence of root u and when qu is coprime with M for $q \in \{1, 2, 3, \ldots, N-1\}$. One way to ensure that the co-prime condition is met is to set $u = 1$, and M to a prime number that is not smaller than N. As the prime number M is also an odd number, the ZC sequence $\mathbf{g}$ is such that

$$g[m] = \exp\left(-\mathrm{j}\frac{\pi m\,(m+1)}{M}\right). \tag{31}$$

The subsampling design problem is solved when such a $\mathbf{g}$ can also be expressed in the form of (26).

We determine conditions on M and N by setting $\mathbf{g}$ in (31) to the one in (26). We observe that the phase of the $g[m]$ in (26) is $-2\pi c[m]/N$, while the phase of $g[m]$ in (31) is $-\pi m(m+1)/M$. The two vectors in (26) and (31) are equal when

$$\frac{2\pi c[m]}{N} = \frac{\pi m\,(m+1)}{M} + 2\pi i_m,\ \forall m \in \{0, 1, 2, \ldots, M-1\}, \tag{32}$$

for some integers $\{i_m\}_{m=0}^{M-1}$. Equivalently,

$$c[m] = \frac{m\,(m+1)\,N}{2\,M} + N i_m. \tag{33}$$

Note that $c[m]$ has to be an integer in $\{0, 1, 2, \ldots, N-1\}$ as it models the circulant shift applied at the TX for the m^{th} channel measurement. It can be observed that a circulant shift of N is equivalent to a zero circulant shift. As $N i_m$ is an integer multiple of N, it does not contribute to $c[m]$ in (33). Therefore, for $c[m]$ to be an integer, we set $M = N$ in (33) to obtain

$$c[m] = \left[\frac{m\,(m+1)}{2}\right]_{\mathrm{mod}\,N}. \tag{34}$$

The subsampling coordinates in partial 2D-DFT CS is then $\Omega = \{(0, c[0]), (1, c[1]), \ldots (M-1, c[M-1])\}$. Such a subsampling technique achieves the smallest coherence under the constraints in our problem.

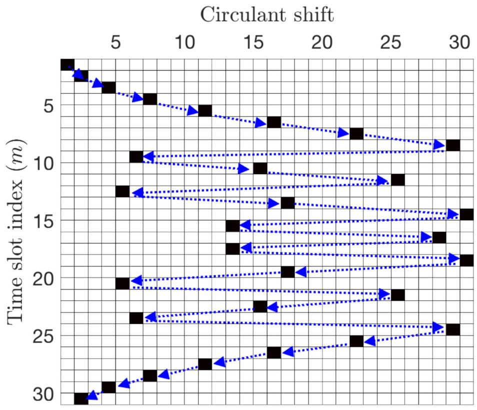

(a) Optimized binary subsampling matrix and the corresponding trajectory for $M = N = 31$.

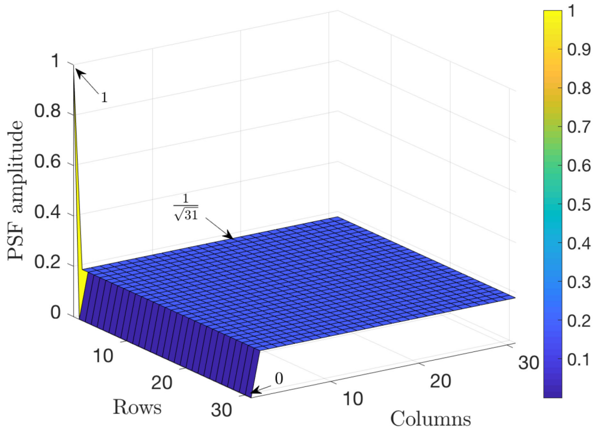

(b) PSF of the optimized subsampling matrix in Fig. 5(a).

Fig. 5. The proposed trajectory goes through the 2D-coordinates marked in black in Fig. 5(a). These coordinates are derived using our ZC-based design. For any feasible trajectory, the first column of the PSF is $\sqrt{M/N}\mathbf{e}_{0,M}$. With the proposed trajectory, we observe from Fig. 5(b) that the remaining columns of the PSF have a constant amplitude of $1/\sqrt{M}$. Such a trajectory achieves the smallest possible coherence in partial 2D-DFT CS under the space-time sampling constraint.

We would like to mention that our result is valid when M is prime and when $M = N$. Optimizing subsampling for other settings is an interesting research direction. In this paper, the RX uses a fixed $N-$length ZC sequence for quasi-omnidirectional reception. This sequence should not be confused with the $M-$length ZC sequence at the TX, which is used to optimize the circulant shifts for efficient CCS.

The optimized binary subsampling matrix and the corresponding PSF for $M = 31$ are shown in Fig. 5(a) and Fig. 5(b). We explain the impact of the PSF $\tilde{\mathbf{B}}$ on target detection by considering the OMP algorithm in a noiseless setting. The first step of the OMP computes $\mathbf{p} = \mathbf{A}^* \mathbf{y}(\rho, \delta)$, and then finds the index that maximizes $|\mathbf{p}|$. Due to the partial 2D-DFT nature of the CS matrix, it can be shown that $\mathbf{p}$ is also the vector version of $\tilde{\mathbf{Z}}(\delta) \circledast \tilde{\mathbf{B}}/\sqrt{MN}$, where $\circledast$ denotes the 2D-circular convolution operation [23]. The first step of the OMP succeeds when the index that maximizes $|\tilde{\mathbf{Z}}(\delta) \circledast \tilde{\mathbf{B}}|$ also maximizes the masked Doppler-angle matrix $|\tilde{\mathbf{Z}}(\delta)|$. From the 2D-circular convolution, it can be observed that every entry of $\tilde{\mathbf{Z}}(\delta) \circledast \tilde{\mathbf{B}}$

is a mixture of the original sparse components in $\tilde{\mathbf{Z}}(\delta)$. For any feasible trajectory, the PSF $\tilde{\mathbf{B}}$ has $M-1$ zeros in the first column. As a result, it follows that the sparse components in the same Doppler bin do not interfere with each other in $\tilde{\mathbf{Z}}(\delta) \circledast \tilde{\mathbf{B}}$. The components in the same angle bin, however, interfere with each other in $\tilde{\mathbf{Z}}(\delta) \circledast \tilde{\mathbf{B}}$. The optimized trajectory minimizes the PSF amplitude to reduce this interference, and achieves better performance than random trajectory-based CS.

We explain guarantees on CS-based reconstruction using the optimized trajectory. As $|\mathbf{U}_M \mathbf{g}^q| = \mathbf{1}$ with our construction, we observe from (28) and (23) that $\mu = 1/\sqrt{M}$. This is also $1/\sqrt{N}$ as $M = N$ with our design. Prior work has shown that the solution to the CS problem, in a noiseless setting, is a unique K sparse vector when $K < 0.5(1 + 1/\mu)$ [39]. Furthermore, the OMP algorithm can recover the K sparse coefficients under this condition [40]. As $\mu = 1/\sqrt{N}$ with our design, the proposed partial 2D-DFT CS technique that acquires subsamples defined by (34) can recover

$$K < \frac{1}{2}\left(1 + \sqrt{N}\right) \tag{35}$$

targets in the Doppler-angle space. In the simulations section, we will show that the OCCS-JCR with the designed subsampling trajectory achieves better radar detection performance than the RCCS-JCR with random subsampling trajectory.

V. ADAPTIVE JCR DESIGN

In this section, we quantify the JCR trade-off between radar and communication for an adaptive combined waveform-beamfoming design using MSE-based metrics. We first describe the NMSE metric for radar, followed by the DMSE metric for communication. Additionally, we also present a MSE-based adaptive combined waveform-beamforming design for the mmWave automotive JCR.

A. Radar Performance Metric

We use the NMSE metric to evaluate the performance of the CS-based radar channel estimation algorithm for our adaptive JCR design. The MSE-based metric is usually employed for evaluating the radar target estimation performance [41], [42]. NMSE is a stronger metric than probability of detection for SRR/MRR target estimation problem because it captures the additional phase and amplitude information. This additional phase and magnitude information is important for target classification, tracking, and data association. There is also a relation between NMSE and probability of detection metrics. A low NMSE value indicates a high probability of detection. A non-negative NMSE in the logarithmic scale indicates close to zero probability of detection.

Without loss of generality, we assume the average target channel power as one. The NMSE metric for a true Doppler-angle domain radar channel $\tilde{\mathbf{h}} = \mathrm{vec}(\tilde{\mathbf{H}})$ and the estimated Doppler-angle domain radar channel $\tilde{\mathbf{h}}_{\mathrm{est}}$ is defined as

$$\mathrm{NMSE}(\rho, \delta) \triangleq \frac{1}{K}\mathbb{E}\left[||\tilde{\mathbf{h}} - \tilde{\mathbf{h}}_{\mathrm{est}}(\rho, \delta)||^2\right], \tag{36}$$

where K is the number of targets.

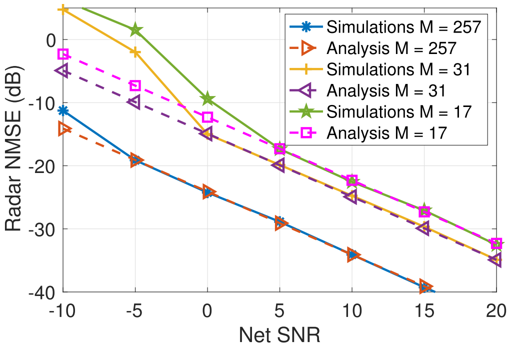

Fig. 6. Comparison between the radar NMSE obtained using analysis in (37) and using simulations with varying net SNR for a single-target scenario. The analytical NMSE closely matches with those of simulations above a certain SNR value that decreases with increasing M.

The NMSE for estimating the masked Doppler-angle channel vector $\tilde{\mathbf{z}}(\delta)$ in (20) corresponding to the dominant channel taps using the optimized sampling trajectory in (34) and the OMP estimation can be approximated similar to the NMSE derivation in [43]. From (3) and (14), we see that the amplitude of all the diagonal elements in $\mathbf{\Lambda}(\delta)$ is $\sqrt{N\delta_{\mathrm{r}}}$ except the first one. Therefore, denoting $\mathbf{A}_{\mathrm{S}}$ as the matrix formed by the support columns (defined as the final set of dominant columns chosen from the dictionary), the pseudoinverse of matrix $\mathbf{A}_{\mathrm{S}}$ as $\mathbf{A}_{\mathrm{S}}^{+} = (\mathbf{A}_{\mathrm{S}}^{*}\mathbf{A}_{\mathrm{S}})^{-1}\mathbf{A}_{\mathrm{S}}^{*}$, the net radar SNR as $\zeta_{\mathrm{net}}(\rho, \delta) = N\delta_{\mathrm{r}}\zeta_{\mathrm{p}}[\rho]$, the NMSE for estimating the Doppler-angle channel vector $\tilde{\mathbf{h}}$ corresponding to the MRR/SRR targets can be approximated similar to [43] as

$$\mathrm{NMSE}(\rho, \delta) \approx \frac{1}{K\zeta_{\mathrm{net}}(\rho, \delta)}\mathrm{Tr}\left[\mathbf{A}_{\mathrm{S}}^{+}(\mathbf{A}_{\mathrm{S}}^{+})^{*}\right], \tag{37}$$

when the probability of success of OMP exceeds a certain threshold. We see from (37) that the NMSE approximation is inversely proportion to the net radar SNR,

Fig. 6 shows the comparison between the NMSE obtained using (37) and the NMSE estimated using simulations with varying net SNR $\zeta_{\mathrm{net}}(\rho, \delta)$ for a single-target scenario. The analytical NMSE decreases with net SNR linearly in the logarithmic scale. The analytical NMSE closely matches with the simulated one above a certain net SNR value. The net SNR value where the analytical and simulations NMSE closely matches decreases with the increase in M. Additionally, the net SNR is a linear function of ρ and an approximate linear function of δ, where the approximation to the linearity is because of the use of phased array architecture and the GS algorithm. Therefore, the radar NMSE metric is generally linear with respect to the optimization variables ρ and δ above a certain net SNR value in the logarithmic scale. In Section VI, we will further explore the relation between the radar NMSE and radar SNR for different multi-target scenarios.

B. Communication Performance Metric

Assuming $s_{m,\ell}[\rho]$ is distributed as $\mathcal{N}(0,1)$, the maximum achievable communication spectral efficiency, r, for a JCR system with $\rho = 0$ and $T_{\mathrm{IFS}} = 0$ with known channel state information at the transmitter (CSIT) is given by

$$r(\delta) = \log_2\left(1 + \delta\zeta_{\mathrm{c}}\right), \tag{38}$$

where $\zeta_{\mathrm{c}} = \mathcal{E}_{\mathrm{s}}|h_{\mathrm{c}}|^2\, N^2/\sigma_{\mathrm{c}}^2$. The channel capacity in bits per second (bps) is given as $C(\delta) = Wr(\delta)$, and the communication minimum MSE (MMSE) per symbol is given as [44, Ch. 7]

$$\mathrm{MMSE}(\delta) = \frac{1}{1+\delta\zeta_{\mathrm{c}}} = 2^{-r(\delta)}, \tag{39}$$

and $\log_2 \mathrm{MMSE}(\delta) = -r(\delta)$ is a logarithmic function of δ. In this paper, we have used the communication performance metric under CSIT conditions to quantify the JCR trade-off between radar and communication for simplicity, similar to [19]. The insights and analysis in this paper can be extended to incorporate the communication performance improvement due to preamble length increase without CSIT, such as by including the effect of channel estimation errors.

As a next step, it will be interesting to see how the communication user also benefits from the preamble length increase, such as by incorporating communication rate reduction due to preamble length increase without CSIT. The insights and analysis in this paper can be extended to incorporate the resulting reduction in communication achievable rate due to preamble length increase by including the effect of pilot-assisted channel estimation errors.

When $\rho > 0$ or and $T_{\mathrm{IFS}} > 0$, the effective maximum achievable communication spectral efficiency, r_{eff}, decreases by a factor of $\alpha[\rho]$

$$\alpha[\rho] = 1 - \frac{M(\rho T_{\mathrm{s}} + T_{\mathrm{IFS}})}{T}, \tag{40}$$

and we define the effective communication spectral efficiency as [44, Ch. 7]

$$r_{\mathrm{eff}}(\rho,\delta) = \alpha[\rho]\log_2\left(1+\delta\zeta_{\mathrm{c}}\right) \text{ bits/s/Hz} \tag{41}$$

$$= r(\delta)^{\alpha[\rho]} \text{ bits/s/Hz}. \tag{42}$$

The effective channel capacity in bps is given as $C_{\mathrm{eff}}(\rho,\delta) = Wr_{\mathrm{eff}}(\rho,\delta)$. We see from (41) that the effective communication spectral efficiency is linearly related to ρ, whereas it is logarithmically related to δ.

C. JCR Performance Metric

The performance metrics of radar and communication are dependent on ρ and δ, as can be seen from (36), (37), and (41). With an increase in δ and a decrease in ρ, the information rate improves, whereas the NMSE for radar channel estimation degrades. Therefore, we focus on optimizing (ρ,δ) for the adaptive mmWave automotive JCR combined waveform-beamforming design. This requires the use of a comparable metric to accurately quantify both radar and communication system performances.

To use an effective scalar communication metric that parallels the concept of the radar NMSE for JCR waveform design optimization, we use an effective distortion MSE communication metric analogous to the distortion metric in the rate-distortion theory [45, Ch. 10], which is defined as [19]

$$\mathrm{DMSE}_{\mathrm{eff}}(\rho,\delta) = 2^{-r_{\mathrm{eff}}(\rho,\delta)} = \left(\mathrm{MMSE}(\delta)\right)^{\alpha[\rho]}. \tag{43}$$

According to (39) and (43), each bit of description reduces the communication distortion MSE by a factor of 2. This implies that as the effective spectral efficiency decreases by a factor of $\alpha[\rho]$, the effective average DMSE increases exponentially by the same factor. Since there is a simple one-to-one relation between effective spectral efficiency and effective DMSE, and the expressions (39) and (43) are analogous to the relation between mean squared-error distortion and rate in the rate distortion theory[45, Ch. 10], it is easy to use and understand. Additionally, this metric is easily extendable to other automotive JCR scenarios, such as the multi-target situation [19], unlike the radar estimation rate metric in [46].

Since the communication DMSE and the radar CRB values are usually substantially different, the log-scale is used to achieve proportional fairness similar to the problem of resource allocation in multi-user communication [44, Ch. 7]. The performance trade-off between communication and radar can then be quantified in terms of the following scalar quantities: $\log(\mathrm{DMSE}_{\mathrm{eff}})$ and $\log(\mathrm{NMSE})$.

D. Weighted-Average Optimization-Based JCR Design

We now formulate an adaptive JCR combined waveform-beamforning design to optimize the preamble block count ρ and the fraction of communication TX gain δ. The JCR performance optimization problem is a multi-objective (two-objective) problem of simultaneously optimizing both the radar performance, in terms of, for example, minimizing the radar NMSE, and the communication performance, in terms of minimizing the effective communication DMSE. We can see from (43) that the communication DMSE metric denoted as $\log \mathrm{DMSE}_{\mathrm{eff}}$ is linear with respect to optimization variables ρ and is logarithmic with the optimization variable δ. The radar NMSE metric denoted as $\log \mathrm{NMSE}$, however, can be non-convex sometimes with respect to the optimization variables, as illustrated in Fig. 6 and later in Section VI. Therefore, the region of achievable JCR objective values with the radar NMSE and communication DMSE pairs corresponding to the feasible values of ρ and δ can be non-convex. Then, the optimal JCR performance is achieved by using the Pareto set of the minimum convex set (termed the convex hull) of the feasible non-convex JCR achievable objective values region, thereby enhancing at least radar NMSE metric without degrading the communication DMSE metric, similar to multi-user communication rate optimization [45, Ch. 15]. Additionally, the convex solution is achievable by using time-sharing or probabilistic occurrence techniques on the extreme points of the convex hull [47].

The scalarization approach is known to achieve a Pareto optimal point for multiple convex objectives [48, Ch. 4]. Therefore, the JCR performance optimization can be formulated as the weighted average of a convex hull of communication and radar MSE-based performance metrics. We denote the scalar communication DMSE metric as $\varphi_{\mathrm{c}}(\mathrm{DMSE}_{\mathrm{eff}}) \triangleq \log \mathrm{DMSE}_{\mathrm{eff}}$ and the scalar radar NMSE metric as $\varphi_{\mathrm{r}}(\mathrm{NMSE}) \triangleq \mathrm{Conv}(\log \mathrm{NMSE})$, which incorporates the convex hull operation with respect to the optimization variables. For a given TX precoder codebook $\mathcal{F}(\delta)$ and a maximum preamble building block count of $P_{\max}$, the JCR performance optimization problem can be formulated as

$$\begin{aligned} \underset{\rho,\delta}{\text{minimize}} \quad & \omega_{\mathrm{r}}\varphi_{\mathrm{r}}(\mathrm{NMSE}) + \omega_{\mathrm{c}}\varphi_{\mathrm{c}}(\mathrm{DMSE}_{\mathrm{eff}}) \\ \text{subject to} \quad & \{T, K, d\} = \text{constants}, \\ & \{\mathbf{f}_m(\delta)\}_{m=0}^{M-1} \in \mathcal{F}(\delta) \\ & 0 \leq \rho \leq P_{\max}, \rho \in \mathbb{Z} \\ & 0 \leq \delta \leq 1, \delta \in \mathbb{R}, \end{aligned} \tag{44}$$

where $\omega_{\mathrm{r}} \geq 0$ and $\omega_{\mathrm{c}} \geq 0$ are the normalizing and weighting factors assigning the priorities for radar and communication tasks, respectively. The radar weighting ω_{r} corresponding to the communication weighting ω_{c} is given by $\omega_{\mathrm{r}} = 1 - \omega_{\mathrm{c}}$. Note that the weights can be adjusted adaptively with respect to the requirements imposed by different scenarios, such as varying radar SNR. Alternatively, the problem in (44) can be modified as minimization of one of the objectives with second as a constraint that would guarantee an acceptable performance for one of the tasks.

VI. NUMERICAL RESULTS

In this section, the numerical results of the proposed adaptive combined waveform-beamforming design for mmWave automotive JCR are presented. First, we evaluate and compare the radar NMSE performance of our leading OCCS-JCR algorithm with RCCS-JCR and RS-JCR techniques at varying distance, target counts, and number of frames/antenna elements. Then, we study the optimal JCR designs for the weighted average based formulation. For illustration purposes, we consider simulation parameters based on the IEEE 802.11ad standard [3], [8] in application to automotive scenarios [1], [26]. We use the OMP algorithm for sparse radar channel reconstruction from the partial 2D-DFT-based measurement model [23]. Under this model, our OMP implementation exploits the fast Fourier transform and results in a lower complexity than the standard counterparts.

Due to a wide variety of automotive applications with different resolution requirements, varying number of antenna elements are used in different automotive radars [49]–[51]. Therefore, the TX and RX antenna arrays are considered to be uniform linear arrays with 17, 31, or 257 elements. Since the recent automotive radar imaging trend is moving towards higher resolution sensing needed for futuristic autonomous driving applications [49], [51], [52], we used the large antenna array size of 257 to meet the best-case resolution requirement. Additionally, a large number of antenna arrays will enable enhanced JCR combined waveform-beamforming design with superior JCR performance. In particular, a larger number of antenna arrays will enable higher antenna array gain for the two-way radar channel sensing in the proposed JCR design (where radar exploits limited preamble duration and small sidelobe beamforming gain), at the cost of only a small reduction in the communication data rate.

Antenna arrays with large antenna aperture have been used in automotive mmWave radars with 192 elements [49], [51] and 400 elements [53], as well as in mmWave communications with 256 elements [54]. The current automotive radars generally use virtual antenna array architecture with a smaller physical size than the traditional phased arrays. The objective of our proposed combined waveform-beamforming design, however, is not to beat the state-of-the-art radar solutions (they might be better if mmWave communication will not be required), but instead to merge communication and radar into a single joint system. Due to the small carrier wavelength at the mmWave band, the phased array of 257 elements (which has a slight increase in the physical size than the cascaded radars with time-division-multiplexing virtual antenna arrays employed in automotive applications [49]) could be used for JCR units mounted on large vehicles (such as a truck) or infrastructures for vehicular applications. Additionally, the physical size would be further reduced at a higher carrier frequency, which is already being considered for both next-generation automotive radars [55] and 6 G communications [56].

We assume 180° FoV, the recipient vehicle distance $d_{\mathrm{c}} =$ 100 m, the preamble building block size of 512 symbols, and a coherent processing interval of 5 ms. Typically near-field effects start ceasing farther away than a few wavelengths of the antenna, as seen in automotive radar field experiments [51], [57], [58]. Therefore, we simulate target ranges above 5 m for evaluating the performance of short-range and medium-range radars. These target ranges fall in the far-field region for $M = 17$ and $M = 31$, and after the reactive near-field region for $M = 257$, where the far-field effects start dominating. The experimental results for our proposed JCR design that includes the distortion effects due to the near-field phenomena for large antenna arrays is left for future work.

A. Radar Performance

In this subsection, we investigate the radar NMSE performance of our proposed CCS-JCR design. We also compare our proposed OCCS-JCR design with optimized subsampling trajectory developed in Section IV versus the RCCS-JCR technique with random sampling. Additionally, we compare the performance of OCCS-JCR and RCCS-JCR designs against the RS-JCR technique.

Figs. 7(a) and (b) show the radar performance of OCCS-JCR and RCCS-JCR for different SNR ζ, number of targets K, frame counts M, and number of TX antenna elements N at $\delta = 0.5$ and $\rho = 2$. In Fig. 7(a) the radar NMSE generally decreases with SNR linearly in the logarithmic scale, as also seen from (37). At high SNR and with a large number of targets, however, we see the saturation effect where the radar NMSE remains constant. The non-linearity of radar NMSE with SNR is also observed at low SNR. In Fig. 7(b), the radar NMSE remains almost the same with increasing number of targets till a critical K. The number of targets that satisfies the constraint in (35), do not suffer from the saturation effect at high SNR. After crossing the critical K, the radar NMSE degrades rapidly, and the critical ζ and K, where the saturation happens, increase with M.

From Figs. 7(a) and (b), we also see that our proposed optimized CCS-JCR always performs the best. The performance gap between the OCCS-JCR and RCCS-JCR grows with increasing SNR. The critical target count, after which the saturation effect occurs, is larger in OCCS-JCR than the RCCS-JCR. Therefore,

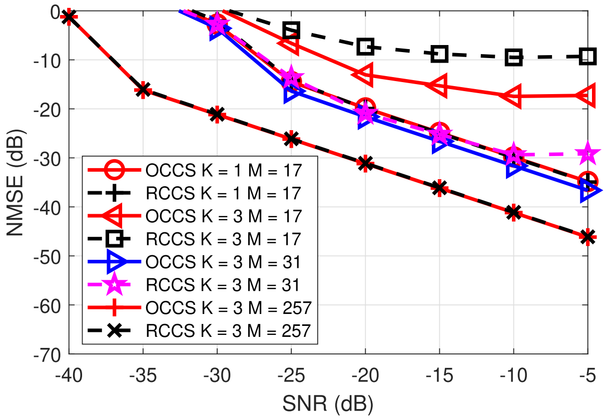

(a) NMSE versus SNR

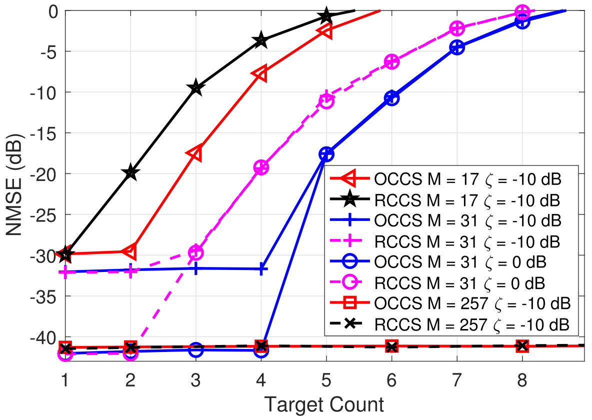

(b) NMSE versus target count

Fig. 7. Comparison between OCCS-JCR and RCCS-JCR for different M, N, SNR (ζ), and K at $\delta = 0.5$ and 1024 training symbols per frame with $\rho = 2$. The OCCS-JCR design with optimized circulant shifts performed better than the RCCS-JCR design, especially at high SNR and target counts.

the performance gap increases with target count between the critical K for RCCS-JCR and the critical K for OCCS-JCR. The performance gap, however, reduces with increasing $M = N$. This reduction with M is because a random trajectory-based sampling matrix results in a small coherence for a large sample space [21]. As a result, RCCS-JCR approaches the performance of OCCS-JCR for a large M.

Fig. 8 shows the comparison between the RS-JCR, RCCS-JCR, and OCCS-JCR for different SNRs and varying target counts at $M = 31$, $\delta = 30/31$, and $\rho = 2$. The OCCS-JCR technique performs the best, followed by RCCS-JCR, and RS-JCR performs the worst. The performance gap between RS-JCR and RCCS-JCR is much larger than the gap between RCCS-JCR and OCCS-JCR at small number of targets. The performance gaps between different JCR approaches start decreasing at large K and high SNR. The poor performance of random switching is observed because the CS matrix in this approach has a high coherence in CS and suffer from SNR loss under the per-antenna power constraint. Furthermore, the RCCS-JCR technique suffers from a low SNR under the per-antenna power constraint [22]. Since our proposed OCCS-JCR technique performs the best, we will use this approach for the numerical analysis on the optimal JCR design.

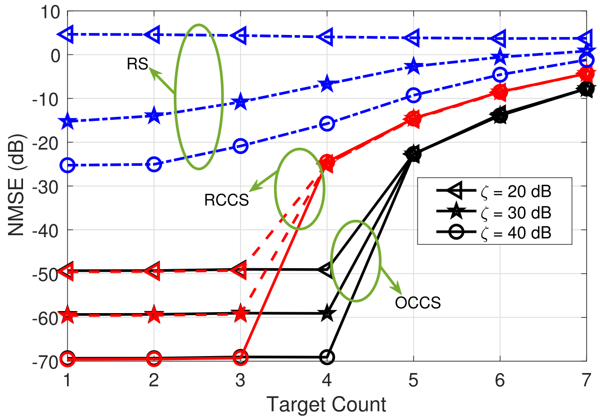

Fig. 8. Comparison between OCCS-JCR, RCCS-JCR, and RS-JCR for different SNRs and varying target counts at $M = 31$, $\delta = 30/31$, and 1024 training symbols per frame. The OCCS-JCR technique performs the best, followed by RCCS-JCR, and RS-JCR performs the worst.

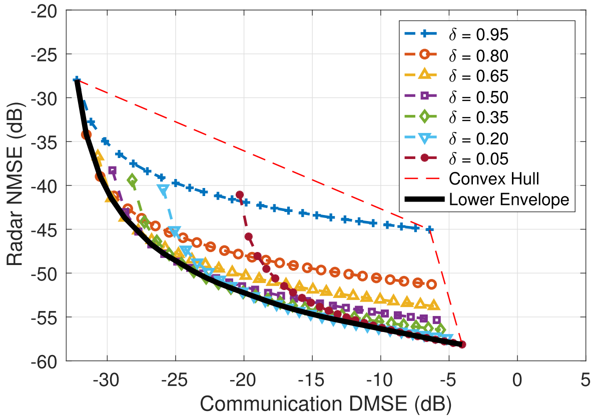

Fig. 9. The radar NMSE and the communication DMSE pairs in the JCR trade-off region with respect to the optimization variable ρ and δ along with their respective convex hulls at $M = N = 257$, -10 dB SNR, and $K = 2$.The achievable 2D-JCR objective values region is obtained by varying both ρ and δ.

B. Optimal JCR Designs

In this subsection, we explore the OCCS-JCR performance trade-off curve between the radar NMSE and the communication NMSE with respect to ρ and δ. Additionally, we investigate the optimal solutions for the weighted average optimization-based JCR design for different SNRs, target counts, and number of frames/antenna elements. We vary the communication weighing $0 \leq \omega_c \leq 1$. The preamble building block length for channel estimation is considered as 512, similar to the IEEE 802.11ad standard. The maximum preamble length is considered as the maximum frame length for $M = 257$, which leads to $P_{\max} = 53$. In our optimization, we do not consider $\delta = 0$ because it is unfavorable for both vehicular communication as well as LRR sensing.

Fig. 9 depicts the performance trade-off between the radar NMSE and communication DMSE metrics with respect to the optimization variables ρ and δ for $M = N =$

257, SNR ζ of -10 dB, $K = 2$, $\rho = [1, 3, \ldots, 53]$, and $\delta = [0.05, 0.20, 0.35, 0.50, 0.65, 0.80, 0.95]$. Since $K \ll M$, and the SNR is high, the JCR trade-off curve between the radar NMSE versus the communication DMSE is convex for a given δ, as explained in Section V. The JCR trade-off curve for a given ρ is almost convex with δ in logarithmic scale. The deviation from the convex approximation is due to the TX phased-array architecture and the phase shift constraint in the GS algorithm to generate the desired $\mathbf{f}_{\mathrm{t}}(\delta)$.

Fig. 9 also illustrates the convex hull of the 2D achievable JCR objective values region, which is the smallest convex set containing the achievable JCR objective values region and can be obtained using computational geometry algorithms [59]. In Fig. 9, we use "convhull" function of MATLAB to obtain the convex hull. Then, we find the optimal solutions for weighted-average optimization in (44) by choosing the lower envelope of the convex hull. The convex hull enables discarding the not so beneficial pairs of the radar NMSE and the communication DMSE in the the 2D feasible JCR achievable objective values region, similar to [19]. Therefore, the convex hull approach will lead to enhanced optimal solutions for JCR designs by achieving lower radar NMSE for a given communication DMSE.

Fig. 10(a) and (b) show the optimal δ and ρ versus ω_{c} for the optimal weighted average-based JCR design with different M and K at an SNR ζ of -10 dB, -35 dB, and -50 dB. For small number of targets, δ increases rapidly with communication weighting. At $\omega_{\mathrm{c}} = 1$, δ converges to 1 with maximum communication spectral efficiency. At $M = 31$ and $K = 7$, however, the optimal δ generally remains constant due to the saturation effect and small communication SNR leading to almost linear relation with δ.

The optimal ρ decreases faster than δ with respect to the communication weighting for large M. This is due to the fact that communication DMSE degrades much slower with δ, whereas it decreases rapidly with ρ. For small M, however, optimal ρ is 1 for even large values of communication weighting because $\alpha[\rho]$ doesn't change much with ρ. At $\omega_{\mathrm{c}} = 1$, ρ converges to minimum preamble length of 512. At $\omega_{\mathrm{c}} = 0$, ρ converges to $P_{\max}$ for all the target scenarios, except for $M = 31$ and $K = 7$ where it converges to a smaller value due to the saturation effect.

Fig. 11(a) and (b) show the optimal radar NMSE and communication NMSE versus communication weightings with different M and K at an SNR (ζ) of -10 dB, -35 dB, and -50 dB. The optimal radar NMSE increases with communication weighting, while the optimal communication DMSE decreases with communication weighting. For $M = 31$, $K = 2$, and $\omega_{\mathrm{c}} = 0.9$, we observe a low radar NMSE of -33.7 dB, while degrading the communication DMSE only by 0.9 dB that corresponds to a slight decrease in the effective communication rate by a factor of 1.06. The saturation effect is observed for $M = 31$ and $K = 7$ for both the optimal radar NMSE and the optimal communication DMSE. The radar NMSE goes beyond 0 dB, and is therefore unusable for automotive radar sensing applications, at $\omega_{\mathrm{c}} = 1$ for ζ of -10 dB and -35 dB, whereas radar is unusable at lower $\omega_{\mathrm{c}} = 0.7$ for ζ of -50 dB and $M = 257$. The weighted average of the radar NMSE and the communication NMSE decreases with increase in M for $K = 2$ and $\zeta = -10$ dB. At $M = 257$, the radar NMSE is much better with decreasing ζ, while the communication NMSE is the same for all ζ at low and high communication weightings. This example demonstrates that we can achieve high-resolution radar channel estimation in the Doppler-angle domain with high accuracy, 180° field of view, and 5 ms CPI, as desired in the MRR/SRR applications [1].

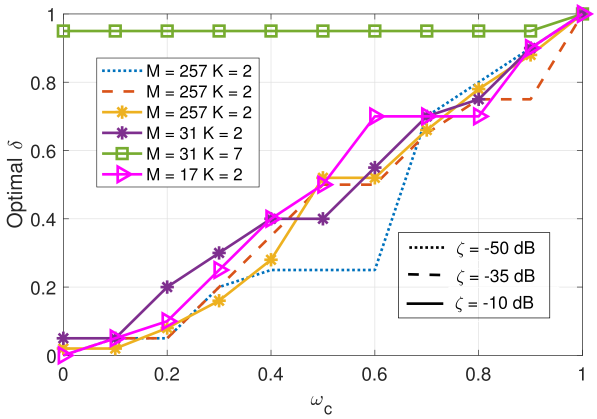

(a) Optimal δ for different weightings

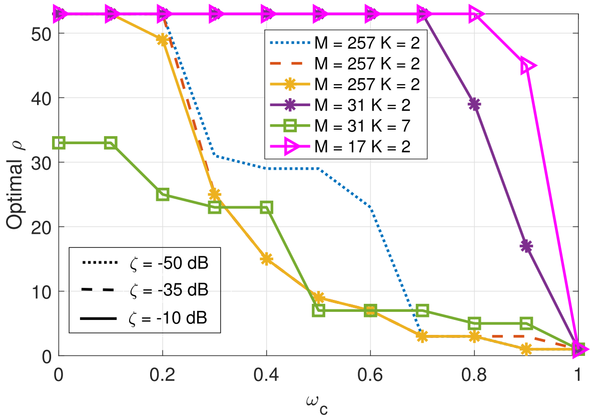

(b) Optimal ρ for different weightings

Fig. 10. Optimal δ increases and optimal ρ decreases with the communication weightings. The optimal ρ decreases faster than δ with respect to the ω_{c} for large M.

VII. CONCLUSIONS

In this paper, we proposed an adaptive and fast combined waveform-beamforming design for the mmWave automotive JCR with a phased-array architecture. Our proposed JCR design achieves a wide field of view by transmitting a fraction of energy along the communication direction and distributing the remaining energy "uniformly" along the other radar sensing directions. Our method uses circulant shifts of the designed JCR beamformer and applies 2D partial Fourier CS to rapidly estimate the radar channel in the Doppler-angle domain. To enhance the radar performance, we also optimize these circulant shifts by minimizing the coherence of the compressed sensing matrix under the sampling constraints of the proposed

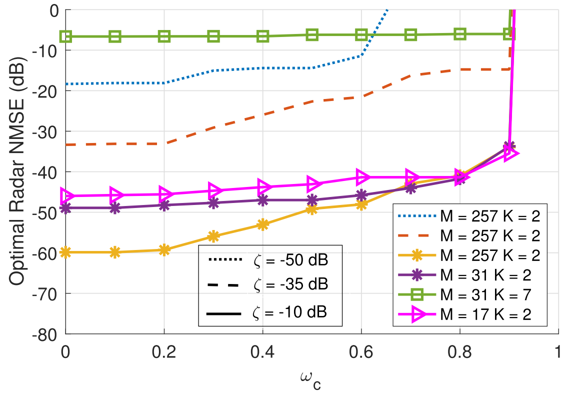

(a) Optimal radar NMSE for different weightings

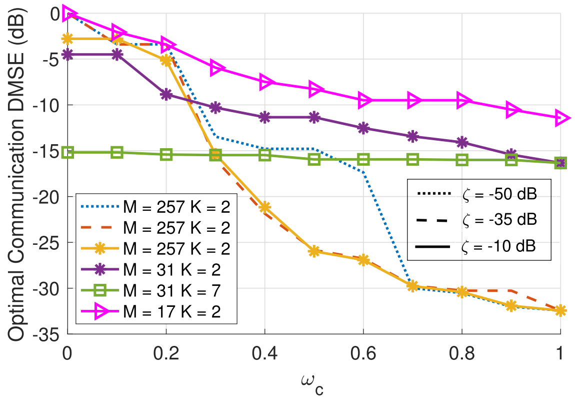

(b) Optimal communication DMSE for different weightings

Fig. 11. Optimal radar NMSE increases and optimal communication DMSE decreases with the communication weightings. This example demonstrates that we can achieve high-resolution SRR/MRR radar channel estimation in the Doppler-angle domain with high accuracy, at the cost of a small reduction in the communication rate.

JCR system. Additionally, we develop a MSE-based weighted average optimization-based JCR design with tunable waveform and beamforming parameters that permits a trade-off between the radar NMSE and the communication DMSE metrics.

The results in the paper demonstrate that our proposed JCR design estimated medium- and short-range automotive radar channels in the range-Doppler angle domain with low NMSE and a wide field of view, at the cost of a small reduction in the communication rate. The proposed JCR design with optimized circulant shifts performed better than the random circulant shifts, especially at high SNR and large target counts. Additionally, we observed the saturation effect in both the approaches at high SNR and target counts. The random switching-based JCR design performed very poorly as compared to our proposed JCR design due to higher coherence of the resultant CS matrix and the low transmit power under the per-antenna power constraint. For large number of frames, the optimal preamble length decreased faster than the optimal fraction of communication TX array gain with respect to the communication weightings. The optimal preamble length and the optimal fraction of communication TX array gain remains almost the same for different SNRs at low and high communication weightings.

The results in this paper can be used to develop low-power, small size, spectrum-efficient, and high-performance mmWave devices that will enable next-generation automotive sensing and communication needs. Future work includes an extension of our work for simultaneous range, velocity, angle-of-arrival, and angle-of-departure estimation. Additionally, our proposed combined waveform-beamforming JCR design can be extended to the UPA scenario. For example, two-dimensional codes based on perfect binary arrays can be used instead of one-dimensional ZC sequences [23] at the RX. Such codes achieve a quasi-omnidirectional beam pattern. The Gerchberg-Saxton algorithm can be used with the 2D-DFT to construct the JCR beamformer at the TX. Finally, the concept of space-time trajectory can be extended to the UPA setting by applying 2D-circulant shifts of the JCR beamformer. In this case, the trajectory traverses over a third-order space-time tensor. Here, two modes of the tensor correspond to the spatial dimension (azimuth, elevation) and the third mode corresponds to the time dimension. It would also be interesting to experimentally evaluate the performance of our proposed JCR design using a measurement platform similar to [58].

ACKNOWLEDGMENT

The authors would like to thank Prof. Sergiy A. Vorobyov of Aalto University, Finland, for discussions regarding the adaptive JCR design.

REFERENCES

[1] S. M. Patole, M. Torlak, D. Wang, and M. Ali, “Automotive radars: A review of signal processing techniques,” *IEEE Signal Process. Mag.*, vol. 34, no. 2, pp. 22–35, Mar. 2017.

[2] J. Choi, V. Va, N. Gonzalez-Prelcic, R. Daniels, C. R. Bhat, and R. W. Heath, “Millimeter-wave vehicular communication to support massive automotive sensing,” *IEEE Commun. Mag.*, vol. 54, no. 12, pp. 160–167, Dec. 2016.

[3] *LAN Wireless Medium Access Control (MAC) and Physical Layer (PHY) Specifications. Amendment 3: Enhancements for Very High Throughput in the 60 GHz Band*, IEEE Standard 802.11ad, 2012.

[4] K. V. Mishra, M. R. B. Shankar, V. Koivunen, B. Ottersten, and S. A. Vorobyov, “Toward millimeter-wave joint radar communications: A signal processing perspective,” *IEEE Signal Process. Mag.*, vol. 36, no. 5, pp. 100–114, Sep. 2019.

[5] D. Ma, N. Shlezinger, T. Huang, Y. Liu, and Y. C. Eldar, “Joint radar-communication strategies for autonomous vehicles: Combining two key automotive technologies,” *IEEE Signal Process. Mag.*, vol. 37, no. 4, pp. 85–97, Jul. 2020.

[6] S. H. Dokhanchi, M. R. B. Shankar, T. Stifter, and B. Ottersten, “Multi-carrier phase modulated continuous waveform for automotive joint radar-communication system,” in *Proc. Int. Workshop Signal Process. Adv. Wireless Commun.*, Jun. 2018, pp. 1–5.

[7] A. Hassanien, M. G. Amin, Y. D. Zhang, and F. Ahmad, “Signaling strategies for dual-function radar communications: An overview,” *IEEE Aerosp. Electron. Syst. Mag.*, vol. 31, no. 10, pp. 36–45, Oct. 2016.

[8] P. Kumari, J. Choi, N. González-Prelcic, and R. W. Heath, “IEEE 802.11ad-based radar: An approach to joint vehicular communication-radar system,” *IEEE Trans. Veh. Technol.*, vol. 67, no. 4, pp. 3012–3027, Apr. 2018.

[9] E. Grossi, M. Lops, L. Venturino, and A. Zappone, “Opportunistic radar in IEEE 802.11ad networks,” *IEEE Trans. Signal Process.*, vol. 66, no. 9, pp. 2441–2454, May 2018.

[10] G. R. Muns, K. V. Mishra, C. B. Guerra, Y. C. Eldar, and K. R. Chowdhury, “Beam alignment and tracking for autonomous vehicular communication using IEEE 802.11ad-based radar,” in *Proc. IEEE Conf. Comput. Commun. Workshops*, Apr. 2019, pp. 535–540.

[11] P. Kumari, M. E. Eltayeb, and R. W. Heath, "Sparsity-aware adaptive beamforming design for IEEE 802.11ad-based joint communication-radar," in *Proc. IEEE Radar Conf.*, Apr. 2018, pp. 0 923–0928.

[12] J. A. Zhang, X. Huang, Y. J. Guo, J. Yuan, and R. W. Heath, "Multibeam for joint communication and radar sensing using steerable analog antenna arrays," *IEEE Trans. Veh. Technol.*, vol. 68, no. 1, pp. 671–685, Jan. 2019.

[13] F. Liu, W. Yuan, C. Masouros, and J. Yuan, "Radar-assisted predictive beamforming for vehicular links: Communication served by sensing," *IEEE Trans. Commun.*, vol. 19, no. 11, pp. 7704–7719, Nov. 2020.

[14] F. Liu, C. Masouros, A. P. Petropulu, H. Griffiths, and L. Hanzo, "Joint radar and communication design: Applications, state-of-the-art, and the road ahead," *IEEE Trans. Commun.*, vol. 68, no. 6, pp. 3834–3862, Feb. 2020.

[15] P. Kumari, K. U. Mazher, A. Mezghani, and R. W. Heath, "Low resolution sampling for joint millimeter-wave MIMO communication-radar," in *Proc. IEEE Stat. Signal Process. Workshop*, Jun. 2018, pp. 193–197.

[16] M. A. Richards, *Fundamentals of Radar Signal Processing*. New York, NY, USA: McGraw-Hill, 2005.

[17] H. Rohling and M.-M. Meinecke, "Waveform design principles for automotive radar systems," in *Proc. CIE Int. Conf. Radar*, Oct. 2001, pp. 1–4.

[18] L. Li, K. Josiam, and R. Taori, "Feasibility study on full-duplex wireless millimeter-wave systems," in *Proc. IEEE Int. Conf. Acoust., Speech Signal Process.*, May 2014, pp. 2769–2773.

[19] P. Kumari, S. A. Vorobyov, and R. W. Heath, "Adaptive virtual waveform design for millimeter-wave joint communication-radar," *IEEE Trans. Signal Process.*, vol. 68, pp. 715–730, Nov. 2019.

[20] L. Dai, B. Wang, Y. Yuan, S. Han, C. I, and Z. Wang, "Non-orthogonal multiple access for 5G: Solutions, challenges, opportunities, and future research trends," *IEEE Commun. Mag.*, vol. 53, no. 9, pp. 74–81, Sep. 2015.

[21] H. Rauhut, "Compressive sensing and structured random matrices," *Theor. Found. Numer. Methods Sparse Recovery*, vol. 9, pp. 1–92, 2010.

[22] P. Kumari, N. J. Myers, S. A. Vorobyov, and R. W. Heath, "A combined waveform-beamforming design for millimeter-wave joint communication-radar," in *Proc. Asilomar Conf. Signals, Syst. Comput.*, 2019, pp. 1422–1426.

[23] N. J. Myers, A. Mezghani, and R. W. Heath, "FALP: Fast beam alignment in mmWave systems with low-resolution phase shifters," *IEEE Trans. Commun.*, vol. 67, no. 12, pp. 8739–8753, Dec. 2019.

[24] K. Li, L. Gan, and C. Ling, "Convolutional compressed sensing using deterministic sequences," *IEEE Trans. Signal Process.*, vol. 61, no. 3, pp. 740–752, Feb. 2012.

[25] W. Liu, T. Wei, Y. Huang, C. Chan, and S. Jou, "All-digital synchronization for SC/OFDM mode of IEEE 802.15.3c and IEEE 802.11ad," *IEEE Trans. Circuits Syst. I Regular Papers*, vol. 62, no. 2, pp. 545–553, Feb. 2015.

[26] J. Hasch, E. Topak, R. Schnabel, T. Zwick, R. Weigel, and C. Waldschmidt, "Millimeter-wave technology for automotive radar sensors in the 77 GHz frequency band," *IEEE Trans. Microw. Theory Techn.*, vol. 60, no. 3, pp. 845–860, Mar. 2012.

[27] R. W. Gerchberg, "A practical algorithm for the determination of phase from image and diffraction plane pictures," *Optik*, vol. 35, pp. 237–246, 1972.

[28] N. J. Myers, J. Kaleva, A. Tölli, and R. W. Heath, "Message passing-based link configuration in short range millimeter wave systems," *IEEE Trans. Commun.*, vol. 68, no. 6, pp. 3465–3479, Jun. 2020.

[29] J. Ziniel and P. Schniter, "Dynamic compressive sensing of time-varying signals via approximate message passing," *IEEE Trans. Signal Process.*, vol. 61, no. 21, pp. 5270–5284, Nov. 2013.

[30] V. Va, T. Shimizu, G. Bansal, and R. W. Heath Jr., "Millimeter wave vehicular communications: A survey," *Found Trends Netw.*, vol. 10, no. 1, pp. 1–118, 2016.

[31] R. W. Heath, N. González-Prelcic, S. Rangan, W. Roh, and A. M. Sayeed, "An overview of signal processing techniques for millimeter wave MIMO systems," *IEEE J. Sel. Top. Signal Process.*, vol. 10, no. 3, pp. 436–453, Apr. 2016.

[32] J. Wang *et al.*, "Beam codebook based beamforming protocol for multi-Gbps millimeter-wave WPAN systems," *IEEE J. Sel. Areas Commun.*, vol. 27, no. 8, pp. 1390–1399, Oct. 2009.

[33] M. Lustig, D. L. Donoho, J. M. Santos, and J. M. Pauly, "Compressed sensing MRI," *IEEE Signal Process. Mag.*, vol. 25, no. 2, pp. 72–82, Mar. 2008.

[34] E. J. Candes, Y. C. Eldar, D. Needell, and P. Randall, "Compressed sensing with coherent and redundant dictionaries," *Appl. Comput. Harmon. Anal.*, vol. 31, no. 1, pp. 59–73, 2011.

[35] M. Lustig, D. Donoho, and J. M. Pauly, "Sparse MRI: The application of compressed sensing for rapid MR imaging," *Magn. Reson. Med. Official J. Int. Soc. Magn. Reson. Med.*, vol. 58, no. 6, pp. 1182–1195, 2007.

[36] V. M. Patel, G. R. Easley, D. M. Healy Jr., and R. Chellappa, "Compressed synthetic aperture radar," *IEEE J. Sel. Top. Signal Process.*, vol. 4, no. 2, pp. 244–254, Apr. 2010.

[37] D. Chu, "Polyphase codes with good periodic correlation properties (corresp.)," *IEEE Trans. Inf. Theory*, vol. 18, no. 4, pp. 531–532, Jul. 1972.

[38] H. D. Luke, "Sequences and arrays with perfect periodic correlation," *IEEE Trans. Aerosp. Electron. Syst.*, vol. 24, no. 3, pp. 287–294, May 1988.

[39] M. F. Duarte and Y. C. Eldar, "Structured compressed sensing: From theory to applications," *IEEE Trans. Signal Process.*, vol. 59, no. 9, pp. 4053–4085, Sep. 2011.

[40] T. T. Cai and L. Wang, "Orthogonal matching pursuit for sparse signal recovery with noise," *IEEE Trans. Inf. Theory*, vol. 57, no. 7, pp. 4680–4688, Jun. 2011.

[41] Y. Yang and R. S. Blum, "MIMO radar waveform design based on mutual information and minimum mean-square error estimation," *IEEE Trans. Aerosp. Electron. Syst.*, vol. 43, no. 1, pp. 330–343, May 2007.

[42] T. Naghibi and F. Behnia, "MIMO radar waveform design in the presence of clutter," *IEEE Trans. Aerosp. Electron. Syst.*, vol. 47, no. 2, pp. 770–781, Apr. 2011.

[43] G. Tan, B. Wu, and T. Herfet, "Performance analysis of OMP-based channel estimations in mobile OFDM systems," *IEEE Trans. Wireless Commun.*, vol. 17, no. 5, pp. 3459–3473, May 2018.

[44] R. W. Heath Jr. and A. Lozano, *Foundations of MIMO Communication*. Cambridge, U.K.: Cambridge Univ. Press, 2019.

[45] T. M. Cover and J. A. Thomas, *Elements of Information Theory*. Hoboken, NJ, USA: Wiley, 2012.

[46] D. W. Bliss, "Cooperative radar and communications signaling: The estimation and information theory odd couple," in *Proc. IEEE Radar Conf.*, May 2014, pp. 50–55.

[47] J. Brehmer, *Utility Maximization in Nonconvex Wireless Systems*. Springer Sci. Bus. Media, vol. 5, 2012.

[48] S. Boyd and L. Vandenberghe, *Convex Optimization*. Cambridge, U.K.: Cambridge Univ. Press, 2004.

[49] K. Ramasubramanian and B. Ginsburg, "Awr1243 sensor: Highly integrated 76-81-GHz radar front-end for emerging ADAS applications," *Texas Instrum. White Paper*, 2017.

[50] INRAS product-Radarbook, [Online]. Available: http://www.inras.at/en/home.html

[51] V. Giannini *et al.*, "A 192-virtual-receiver 77/79 GHz GMSK code-domain MIMO radar system-on-chip," in *Proc. IEEE Int. Solid- State Circuits Conf.*, Mar. 2019, pp. 164–166.

[52] J. Dickmann *et al.*, "Automotive radar the key technology for autonomous driving: From detection and ranging to environmental understanding," in *Proc. IEEE Radar Conf.*, 2016, pp. 1–6.

[53] T. Yamawaki and S. Yamano, "60-GHz millimeter-wave automotive radar," *Fujitsu Ten Tech. J.*, vol. 11, no. 3, 1998.

[54] S. Zihir, O. D. Gurbuz, A. Kar-Roy, S. Raman, and G. M. Rebeiz, "60-GHz 64- and 256-elements wafer-scale phased-array transmitters using full-reticle and subreticle stitching techniques," *IEEE Trans. Microw. Theory Techn.*, vol. 64, no. 12, pp. 4701–4719, Dec. 2016.

[55] F. Norouzian, E. G. Hoare, E. Marchetti, M. Cherniakov, and M. Gashinova, "Next generation, low-THz automotive radar - the potential for frequencies above 100 GHz," in *Proc. Int. Radar Symp.*, 2019, pp. 1–7.

[56] T. S. Rappaport *et al.*, "Wireless communications and applications above 100 GHz: Opportunities and challenges for 6 G and beyond," *IEEE Access*, vol. 7, pp. 78 729–78 757, Jun. 2019.

[57] P. Kumari, A. Mezghani, and R. W. Heath, "A low-resolution ADC proof-of-concept development for a fully-digital millimeter-wave joint communication-radar," in *Proc. IEEE Int. Conf. Acoust., Speech Signal Process.*, May 2020, pp. 8619–8623.

[58] P. Kumari, A. Mezghani, and R. W. Heath, "JCR70: A low-complexity millimeter-wave proof-of-concept platform for a fully-digital SIMO joint communication-radar," *IEEE Open J. Veh. Technol.*, Mar. 2021.

[59] F. P. Preparata and M. I. Shamos, *Computational Geometry: An Introduction*. Springer Sci. Bus. Media, 2012.

Preeti Kumari (Member, IEEE) received the B.Tech. degree in electronics and telecommunication engineering from the Shri Guru Gobind Singhji Institute of Engineering and Technology, Nanded, India, in 2009, and the M.S. and Ph.D. degrees in electrical and computer engineering from The University of Texas at Austin, Austin, TX, USA, in 2016 and 2020, respectively. She is currently a Senior Engineer with Qualcomm, San Diego, CA, USA. During the summer of 2018, 2016, and 2015, she was an Intern with Qualcomm, San Diego, CA, USA, Intel Labs, Hillsboro, OR, USA, and National Instruments, Austin, TX, USA. From 2009 to 2013, she was a Scientist with Indian Space Research Organization, Ahmedabad, India. Her research interests include system design, signal processing applications, and hardware implementation aspects of radars, wireless communications, and joint communication-radar.

Nitin Jonathan Myers (Member, IEEE) received the B.Tech. and M.Tech. degrees in electrical engineering from the Indian Institute of Technology (IIT) Madras, Chennai, India, in 2016, and the Ph.D. degree in electrical and computer engineering from The University of Texas at Austin (UT Austin), Austin, TX, USA, in 2020. He is currently an Assistant Professor with the Delft Center for Systems and Control, Delft University of Technology (TU Delft), Delft, The Netherlands. Prior to joining TU Delft, he was a Senior Engineer with Samsung Semiconductor Inc., San Diego, CA, USA. His research interests include optimization and multidimensional signal processing, with applications to communications and sensing.

He was Exemplary Reviewer of the IEEE TRANSACTIONS ON COMMUNICATIONS in 2019, and the IEEE WIRELESS COMMUNICATIONS LETTERS in 2018. He was the recipient of DAAD WISE Scholarship in 2014, and Silver Medal, Institute Merit Prize in 2016 during his undergraduate days at IIT Madras. At UT Austin, he was the recipient of University Graduate Continuing Fellowship 2019-2020, 2018 and 2019 ECE Research Awards, and the 2018 ECE Professional Development Award from the Cockrell School of Engineering. He mentored a team of undergraduates that was the recipient of the First Runner-Up Prize in IEEE ICASSP 2020 video contest.

Robert W. Heath (Fellow, IEEE) received the B.S. and M.S. degrees in electrical engineering from the University of Virginia, Charlottesville, VA, USA, in 1996 and 1997, respectively, and the Ph.D. degree in electrical engineering from Stanford University, Stanford, CA, USA, in 2002. From 1998 to 2001, he was a Senior Member of the Technical Staff then a Senior Consultant with Iospan Wireless Inc., San Jose, CA, USA, where he worked on the design and implementation of the physical and link layers of the first commercial MIMO-OFDM communication system. From 2002 to 2020, he was with The University of Texas at Austin, Austin, TX, USA, most recently the Cockrell Family Regents Chair of engineering and the Director of UT SAVES. He is currently a Distinguished Professor with North Carolina State University, Raleigh, NC, USA. He is also the President and the CEO of MIMO Wireless Inc. He authored *Introduction to Wireless Digital Communication* (Prentice Hall, 2017) and *Digital Wireless Communication*: Physical Layer Exploration Lab Using the NI USRP (National Technology and Science Press, 2012), and coauthored *Millimeter Wave Wireless Communications* (Prentice Hall, 2014) and *Foundations of MIMO Communication* (Cambridge University Press, 2018). He is currently the Editor-in-Chief of the IEEE SIGNAL PROCESSING MAGAZINE and is a Member-at-large of the IEEE Communications Society Board of Governors.

He was a Distinguished Lecturer and a Member of the Board of Governors in IEEE Signal Processing Society. In 2017, he was selected as a Fellow of the National Academy of Inventors. He is also a licensed Amateur Radio Operator, a Private Pilot, a registered Professional Engineer in Texas. He has been a co-author of a number award winning conference and journal papers, including recently 2016 IEEE Communications Society Fred W. Ellersick Prize, 2016 IEEE Communications and Information Theory Societies Joint Paper Award, 2017 Marconi Prize Paper Award, 2019 IEEE Communications Society Stephen O. Rice Prize, and 2020 IEEE Signal Processing Society Overview Paper Award. He was the recipient of 2017 EURASIP Technical Achievement Award and 2019 IEEE Kiyo Tomiyasu Award.